HHS Public Access

Author manuscript

Nat Metab. Author manuscript; available in PMC 2023 July 19.

Published in final edited form as:

Nat Metab. 2023 January ; 5(1): 41–60. doi:10.1038/s42255-022-00711-9.

CYTOSOLIC ALDOSE METABOLISM CONTRIBUTES TO PROGRESSION FROM CIRRHOSIS TO HEPATOCARCINOGENESIS

Z Oaks[#1,3,*], **A Patel**[#1,3,*], **N Huang**[1,3], **G Choudhary**[1,3], **T Winans**[1,3], **T Faludi**[1], **D Krakko**[1], **M Duarte**[1], **J Lewis**[1], **Beckford**[1], **S Blair**[1], **R Kelly**[1], **SK Landas**[4], **FA Middleton**[5], **JM Asara**[6], **SK Chung**[7], **DR Fernandez**[1,3], **K Banki**[4], **A Perl**[1,2,3,#]

[1]Department of Medicine, State University of New York, Norton College of Medicine, Syracuse, New York 13210, USA

[2]Department of Microbiology and Immunology, State University of New York, Norton College of Medicine, Syracuse, New York 13210, USA

[3]Department of Biochemistry and Molecular Biology, State University of New York, Norton College of Medicine, Syracuse, New York 13210, USA

[4]Department of Pathology, State University of New York, Norton College of Medicine, Syracuse, New York 13210, USA

[5]Department of Neuroscience, State University of New York, Norton College of Medicine, Syracuse, New York 13210, USA

[6]Division of Signal Transduction, Department of Medicine, Beth Israel Deaconess Medical Center, Harvard Medical School, Boston, Massachusetts, USA

[7]Faculty of Medicine, Macau University of Science and Technology, Taipa, Macau, China

[#] These authors contributed equally to this work.

Abstract

Oxidative stress modulates carcinogenesis in the liver. However, direct evidence for metabolic control of oxidative stress during pathogenesis, particularly, of progression from cirrhosis to hepatocellular carcinoma (HCC), has been lacking. Deficiency of transaldolase (TAL), a rate-limiting enzyme of the non-oxidative branch of the pentose phosphate pathway (PPP), restricts growth and predisposes to cirrhosis and HCC in mice and humans. Here, we show that mitochondrial oxidative stress and progression from cirrhosis to HCC and acetaminophen-induced

[#]To whom correspondence should be addressed: Andras Perl, MD/PhD, SUNY, 750 East Adams Street, Syracuse, New York 13210, Phone: (315) 464-4194; Fax: (315) 464-4176, perla@upstate.edu.

[*]These two authors contributed equally to this study.

Author Contributions

APe conceived and designed the study. APe, ZO, APa, NH, JA, TF, DK developed methodology, executed experiments, and analyzed data. MB, SB, JL, MD, and RK acquired the data (bred, genotyped, and provided animals matched for age and gender). DF, TW, and GC designed, executed, and analyzed experiments. SL and KB designed experiments and analyzed data.

Supplementary Materials contain List of Abbreviations and Supplemental Data.

Competing Interests Statement

The authors declare having no competing interests.

liver necrosis are critically dependent on NADPH depletion and polyol buildup by aldose reductase (AR), while this enzyme protects from carbon trapping in the PPP and growth restriction in TAL deficiency. Both TAL and AR are confined to the cytosol, however, their inactivation distorts mitochondrial redox homeostasis in opposite directions. The results suggest that AR acts as a rheostat of carbon recycling and NADPH output of the PPP with broad implications for disease progression from cirrhosis to HCC.

Keywords

transaldolase; aldose reductase; pentose phosphate pathway; polyols; tricarboxylic acid cycle; mitochondrial oxidative stress; cirrhosis; hepatocarcinogenesis; acetaminophen-induced liver failure; body size and weight

INTRODUCTION

HCC is the fifth most common cancer and the third leading cause of cancer-related mortality worldwide [1]. Hepatocyte transformation generally occurs in cirrhotic livers in the setting of oxidative stress [2]. The precise role of oxidative stress in the progression from cirrhosis to HCC or carcinogenesis has been controversial. Oxidative stress has been proposed both as a promoter and inhibitor of carcinogenesis [3]. Along these lines, the availability of principal intracellular antioxidants, such as reduced glutathione (GSH) and NADPH, has been demonstrated to exert pro-carcinogenic [4] and anti-carcinogenic effects [5]. GSH may be synthesized *de novo* from its amino acid precursors or regenerated from its oxidized form, GSSG, at the expense of NADPH [2].

The pentose phosphate pathway (PPP) is considered the principal source of NADPH production in mammalian cells [2]. The PPP was originally formulated based on enzymatic activities and metabolites found in yeast [6]. The PPP fulfills two essential functions: i) the formation of ribose 5-phosphate (R5P) for the synthesis of nucleotides in support of cell growth and proliferation and ii) the formation of NADPH for biosynthetic reactions and maintenance of an intracellular reducing environment. The PPP is composed of two separate, oxidative and non-oxidative, branches. The rate-limiting enzyme of the oxidative branch, glucose 6-phosphate dehydrogenase (G6PD) has been identified as a driver and biomarker of HCC, assuming its permissive role in providing NADPH [7]. Although G6PD mutations represent the most common genetic defect in humans, affecting 400 million people globally [8], complete deficiency of G6PD is not compatible with cell survival [9]. In contrast, mice lacking transaldolase (TAL), a rate limiting enzyme of the non-oxidative branch of the PPP, develop to adulthood with the exception of male infertility due to structural and functional damage of sperm mitochondria [10]. Importantly, the deficiency of TAL also predisposes to HCC both in mice [11] and humans [12, 13].

TAL-deficiency in mice clearly shows that this rate-limiting enzyme of the PPP plays a role in hepatocellular oxidative stress [11] and may account for liver disease of variable severity in children carrying inactivating mutations [14]. The metabolic basis of liver disease in TAL-deficiency is characterized by the accumulation of sedoheptulose 7-phosphate (S7P) and the failure to recycle R5P through the non-oxidative branch, resulting in NADPH and

GSH depletion [11, 14]. Human TAL-deficient lymphoblasts also exhibit S7P accumulation and G6P depletion, indicating a failure to recycle R5P into G6P through the non-oxidative branch of the PPP, thus reducing NADPH production by the oxidative branch [15]. Both in mice [11] and humans [16], TAL deficiency also predisposes to hepatocyte necrosis induced by acetaminophen (APAP), which is the leading cause of acute liver failure worldwide. APAP damages hepatocytes via production of N-acetyl-para-benzoquinone imine, which can be neutralized by conjugation with GSH [17] or reduced back to acetaminophen by NADPH [18].

Of note, hepatomas of TAL-deficient mice overexpress NADPH-dependent aldose reductase (AR) [11]. The profound depletion of NADPH in TAL deficiency may be attributed to the activation of AR that converts the accumulated sugars to polyols at the expense of NADPH. Polyol levels are markedly accumulated in the urine of TALKO mice [19] and patients with TAL deficiency [14], including those with HCC [12, 13]. The accumulation of polyols in the urine is consistent with their osmotic toxicity to hepatocytes [20] and other types of cells [21]. Activation of AR may also contribute to drug resistance of HCC in general [22]. In this study, we provide mechanistic evidence that inactivation of NADPH-dependent AR blocks mitochondrial oxidative stress, polyol accumulation, and liver disease progression from cirrhosis to HCC in mice double-deficient for TAL and AR (DKO). High-resolution mass spectrometry, stable isotope tracing, RNA sequencing, and confirmatory functional studies unveiled carbon sequestration in the non-oxidative branch of the PPP that caused growth restriction, NADPH depletion and restricted substrates for the tricarboxylic acid (TCA) cycle, amino acid, amino sugar, and phospholipid biosynthesis in TAL deficiency. Amongst NADPH-consuming enzymes, AR was strikingly and consistently upregulated on the RNA and protein levels in TALKO mice and TALKO hepatomas [11]. Here, we show that the inactivation of AR reversed NADPH depletion and polyol buildup in the absence of TAL and blocked mitochondrial oxidative stress and liver disease progression from cirrhosis to HCC. DKO mice were resistant to APAP-induced liver necrosis, indicating that normalization of NADPH and blocking of polyol accumulation were protective. Although AR inactivation blocked mitochondrial oxidative stress and liver disease progression from cirrhosis to HCC, it exacerbated carbon sequestration in the PPP and caused further growth restriction. Inactivation of TAL and AR also impacted carbon flux between the PPP and the TCA cycle. Alternatively, knockdown of isocitrate dehydrogenase 2 (IDH2) markedly enhanced the accumulation of S7P in DKO hepatocytes unveiling a crosstalk between the non-oxidative PPP and the TCA cycle upon inactivation of the TAL-AR axis. Thus, our studies show that the cytosolic TAL-AR axis acts as rheostat of NADPH output by a reformulated PPP with broad implications for metabolic reprogramming of body size and disease progression from cirrhosis to hepatocarcinogenesis. However, GSH depletion persisted in DKO mice, which was attributed to metabolism by AR of pyroglutamic acid (PGA), an intermediate in recycling of glutamate for GSH biosynthesis. Therefore, AR plays a direct role both in reversal of NADPH depletion and persistence of GSH depletion in DKO mice. Thus, the elimination of cancer in TALKO mice lacking AR provides a causal, mechanistic insight into hepatocarcinogenesis.

RESULTS

AR deletion restores NADPH and blocks hepatocarcinogenesis and APAP-induced liver failure in TALKO mice

To delineate the role of AR in hepatocarcinogenesis, we genetically inactivated this enzyme in mice deficient of transaldolase (TAL). AR expression was eliminated on the RNA (Supplementary Figure 1) and protein levels, creating mice double deficient for TAL and AR (DKO; Figure 1A). The depletion of NADPH and the reduction of NADPH/NADP ratio in TALKO livers were reversed upon AR inactivation in DKO livers (Figure 1B). NADH and NADH/NAD ratio followed a similar pattern (Figure 1B). GSH depletion of TALKO livers persisted in DKO livers. Interestingly, GSH/GSSG ratio was diminished in DKO livers over wild-type (WT) controls (Figure 1B). Increased pJNK and c-jun expression, which have been documented as oxidative stress-dependent checkpoints of hepatocarcinogenesis in TAL deficiency [11], were corrected by AR inactivation (Figure 1A). However, cirrhosis, which is caused by GSH depletion and responds to treatment with N-acetylcysteine (NAC) in TALKO mice [11] and humans [23], persisted in DKO mice (Figure 1C).

Premature death from hepatocarcinogenesis in TALKO mice at mean age of 74 weeks [11] closely corresponds to the average age of 65 years upon HCC diagnosis in humans [24]. To evaluate the impact of AR deletion on hepatocarcinogenesis, mice were aged to 78 weeks, beyond the mean age of HCC onset at 74 weeks. Macroscopy (Figure 1D) and microscopy of liver pathology (Figure 1E) revealed strikingly increased HCC rates in TALKO mice over WT controls (Figure 1F). However, WT, ARKO, and DKO mice had similar HCC rates, indicating an effective blockade of hepatocarcinogenesis by AR inactivation (Figure 1F). There is considerable heterogeneity in disease progression in mouse models of HCC which is largely dependent on the underlying pathogenesis, such as induction by chemicals, diet, or genetic intervention. Anisonucleosis has been proposed as an early stage of HCC progression [25]. In TALKO mice, 4 stages of hepatocarcinogenesis were delineated which were characterized by 1) anisonucleosis; 2) anisonucleosis with increased mitotic figures; and 3) anisonucleosis with dysplastic nodules as pre-HCC stages; and 4): HCC with macroscopically visible tumor and histological evidence for invasion of normal tissue by pleomorphic and often anaplastic giant hepatocytes. Prevalence of anisonucleosis was increased in TALKO mice over WT, ARKO, and DKO controls (Figure 1G). In the TALKO group there were six mice with stage 2 lesions and 2 mice with stage 3 lesions. In the DKO group, there was 1 mouse with stage 2 lesion and none with stage 3 lesion. None of the WT and ARKO mice had stage 2 or stage 3 lesion. These findings suggest that stages 2 and 3 represent a rapid transitional phase in our model.

TAL-deficiency also predisposes to acetaminophen-induced necrosis in mice [11] and humans [16, 26], the leading cause of acute liver failure in the United States [27]. Acetaminophen damages hepatocytes via production of N-acetyl-para-benzoquinone imine, which can be neutralized by conjugation with GSH [17] or reduced back to acetaminophen by NADPH [18]. DKO mice did not exhibit increased susceptibility to acetaminophen (Figure 1H), indicating that normalization of NADPH alone was protective.

Inactivation of TAL-AR axis synergistically restricts body weight

In stark contrast to their opposing effects on carcinogenesis, inactivation of TAL and AR synergistically restricted weight gain. By 24 weeks of age, WT mice (36.0±3.4g) were 58% larger than DKO mice (22.8±0.6g; p=0.0047; Figure 2A). Weights of TALKO (26.0±0.7 g) and ARKO mice (26.2±0.7 g) were reduced compared to WT controls but increased compared to DKO mice (Figure 2A). To assess hepatomegaly, liver weight was measured and compared to the body weight of each mouse. WT livers were 2.75 ± 0.15% of total body weight. Relative liver weights were increased in TALKO mice at 4.68 ± 0.33% of body weight, indicating a greater hepatosomatic ratio (p=0.0001). Hepatosomatic ratios were also increased at 3.82 ± 0.12% in ARKO mice (p=0.001) and 4.56 ± 0.24% in DKO mice (p=0.00007; Figure 2A). While diminished body size in TAL-deficient mice was predictable given a similar phenotype of growth retardation in children limiting both body size and weight [14], the reduced weight of AR-deficient mice and the synergistic, inhibitory effects of TAL and AR on weight gain were both surprising and dramatic (Figure 2A).

AR distorts the accumulation of NADPH and S7P in opposite directions

High-resolution mass spectrometry revealed that the inactivation of the TAL-AR axis exerted contrasting directionality on metabolic pathways that control body weight and hepatocarcinogenesis, which involved remarkably opposing effects on substrates of the non-oxidative and oxidative branches of the PPP (Extended Data Figure 1A). Unsupervised dendrogram clustering of fold changes of the top 30 metabolites effectively segregated four genotypes (Figure 2B). Partial least squares-discriminant analysis (PLS-DA) sharply distinguished TALKO and WT mice (Figure 2C), requiring only two components (Supplementary Figures 2A and 2B). Volcano plots showed striking accumulation of S7P, sedoheptulose bisphosphate (SBP), octulose 8-phosphate (O8P), octulose bisphosphate (OBP), and erythrose 4-phosphate (E4P) in the non-oxidative branch of the PPP. This contrasted with depletion of the oxidative branch substrates (G6P, gluconate, 2-dehydroxygluconate), NADPH, NADH, amino acid synthesis intermediates (2-keto-isovalerate, N-acetyl-glutamine, and cystathionine), nucleotide and amino sugars (UDP-glucose and UDP-N-acetyl-glucosamine or UDP-GlcNAc), glycerophospholipid precursors (phosphorylcholine and CDP-choline; Figure 2C), and tricarboxylic acid (TCA) cycle metabolites α-ketoglutarate (α-KG), citrate, fumarate, malate, oxaloacetate (OAA).

The metabolome of ARKO livers required four components and greater confidence intervals than TALKO livers for differentiation from WT controls (Figure 2D and Supplementary Figure 3). DKO livers were even less distinct from WT controls as five components and greater confidence intervals were necessary for differentiation (Figure 2E and Supplementary Figure 4). The accumulation of PPP metabolites (S7P, SBP, OBP, E4P, and O8P) was exacerbated, while the depletion of NADPH and NADH was corrected, and the loss of malate and OAA worsened in DKO livers (Extended Data Figure 2).

Pathway analysis unveiled that TAL deficiency most prominently impacted the PPP, glycerophospholipid, and amino acid metabolism (Extended Data Figure 1B). AR deficiency alone had moderate pathway impact (Extended Data Figure 1C). Due to further accumulation of non-oxidative branch metabolites, the PPP emerged as the top driver of

distinction between DKO and WT mice ($p=4\times10^{-7}$; Extended Data Figure 1D). Changes of metabolite concentrations caused by AR inactivation depended on its enzymatic activity, as recombinant AR directly metabolized erythrose, ribose, sedoheptulose, OAA, and PGA, but not ascorbate, S7P, or E4P at the expense of NADPH (Extended Data Figure 1E).

The depletion of NADPH and NADH in TAL deficiency was corrected by AR inactivation in DKO mice (Figure 1B). Stable isotope tracing studies were performed to further substantiate the impact of the TAL-AR axis on NADPH homeostasis (Figure 3A). Along this line, ^{2}H-NADPH production was reduced by 68% in TALKO hepatocytes relative to WT controls (p=0.0135), which was reversed by AR inactivation in hepatocytes labelled with [3-^{2}H]-glucose (Figure 3B). Labeling of TALKO hepatocytes with [1,2-^{13}C]-glucose unveiled a 19-fold greater enrichment of [M1-^{13}C]-S7P and 12-fold greater enrichment of [M2-^{13}C]-S7P in comparison to WT controls (Figure 3C). Similar trends were noted in greater accumulation of [M1-^{13}C]-R5P over [M2-^{13}C]-R5P in TALKO mice (Figure 3C). [M1-^{13}C]-S7P and [M1-^{13}C]-R5P are generated by the oxidative branch, while [M2-^{13}C]-S7P and [M2-^{13}C]-R5P are generated by the non-oxidative branch of the PPP (Figure 3A)[28].These findings suggest that sequestration of carbon by the PPP is primarily mediated by a greater blockade of carbon flux through the oxidative branch. Labeling of primary hepatocyte cultures with [U-^{13}C]-glutamine also showed greater accumulation of [M1-^{13}C]-S7P in the absence of TAL (Figure 3D). In contrast, enrichment of [M1-^{13}C]-G6P and [M2-^{13}C]-G6P was diminished in TALKO hepatocytes labelled with [U-^{13}C]-glutamine (Figure 3D). These findings suggest that sequestration of carbon by the non-oxidative PPP syphons off metabolites from the TCA cycle in TAL deficiency.

AR dampens oxidative stress-driven gene expression in TAL deficiency

Transcriptional control over carcinogenesis by the TAL-AR axis was delineated by RNAseq analyses of livers from disease-free, 14–16-week-old, age-matched female WT, TALKO, ARKO, and DKO mice. Out of 24,606 sequenced RNAs, TAL deficiency impacted 300 genes at false discovery rate (FDR) p value < 0.05 (Supplementary Table 1 and Figure 4A), which involved 46 biological processes (Figure 4B). The mitochondrial electron transport chain (ETC) was most affected due to altered expression of genes encoding complexes I (Ndufa4, Ndufa8, Ndufa13), III (cytochrome c reductase QCR6, QCR8, QCR9), IV (cytochrome c oxidase subunits Cox4i1 and Cox7b) and V (Atp5a1; Supplementary Figure 5). While expression of genes involved in mitochondrial ETC, glycolysis, and glycosylation remained altered, changes in expression of genes involved in vesicular traffic were reversed in DKO mice (Figure 4B). Notably, AR inactivation corrected gene expression changes on the protein level imposed by TAL deficiency on cell proliferation and autophagy (Supplementary Figure 6).

The metabolome-linked RNAseq changes were systematically confirmed at the protein level. Expression of NDUFS3, a pro-oxidant complex I gene [29], was increased in TALKO but not DKO mice (Extended Data Figure 3A). Given this change of the inner mitochondrial membrane, we examined outer mitochondrial membrane proteins, VDAC1 and Bak1, as controls. The expression of both VDAC1 and Bak1 was also increased in TALKO livers. Interestingly, VDAC1 was further enhanced (Extended Data Figure 3B), while Bak1 was

restrained by inactivation of AR (Extended Data Figure 3A). ETC genes, NDUFB8 of complex I, SDHB of complex II, and ATP5A of complex V were similarly over-expressed in TALKO and DKO mice (Extended Data Figure 3B).

In accordance with RNAseq data (Figure 4A), protein levels of redox-sensor NADPH:quinone oxidoreductase 1 (NQO1)[30] were markedly increased in TALKO livers (3.6-fold, p=0.024), diminished in ARKO livers, and moderated in DKO relative to TALKO livers (Extended Data Figure 3A). Unlike NQO1, expression of NADPH-producing enzymes, cytosolic ME1 and mitochondrial IDH2, were increased both in TALKO and DKO mice (Extended Data Figure 3B). Altogether, these findings indicate that expression of genes involved in mitochondrial oxidative stress (NDUFS3, Bak1, NQO1) were moderated, while those connected to carbon trapping in the PPP (GPI1, ME1, IDH2) and mitochondrial mass (VDAC1) persisted in DKO mice (Extended Data Figure 3).

Among genes involved in GSH metabolism, glutaminyl-peptide cyclotransferase (QPCT) RNA (Figure 4A) and protein levels were diminished by 54% in TALKO livers (p=0.015) and by 74% in DKO livers (p=0.003; Extended Data Figure 3B). QPCT catalyzes the formation of PGA [31]. Changes in QPCT mirrored the depletion of PGA in TALKO and DKO mice (Extended Data Figure 4A). As hereby uncovered, PGA was directly metabolized by AR (Extended Data Figure 1E), and it was accumulated in ARKO mice *in vivo* (Extended Data Figure 4A) and *in vitro* (Extended Data Figure 4B), which compromised *de novo* GSH synthesis in [U-^{13}C]-glutamine-labelled hepatocytes of ARKO and DKO mice (Extended Data Figure 4B). PGA is an intermediate in recycling of glutamate for GSH biosynthesis (Extended Data Figure 4C) [32]. Therefore, AR plays a direct role both in the reversal of NADPH depletion and persistence of GSH depletion in DKO mice.

Accumulation of polyols is AR-dependent in TALKO mice

Polyols accumulate in the urine of mice [19] and patients with TAL deficiency [14]. In accordance with the osmotic toxicity of polyols to hepatocytes [20] and other cells [21], they were not accumulated in TALKO hepatocytes (Figure 5A). However, steady-state levels of PPP-derived C5-polyols, such as arabitol/xylitol/ribitol were moderately depleted in ARKO livers (−13.9 ±1.4%; p=0.005) and, to a lesser degree, in DKO livers (−8.1±4.1%; p=0.068); although the changes in DKO mice failed to reach statistical significance (Figure 5A). Steady state levels of sorbitol were unchanged in the liver (Figure 5A). Importantly, AR inactivation completely blocked the accumulation of [M2-^{13}C]-sorbitol in ARKO or DKO hepatocytes labelled with [1,2-^{13}C]-glucose for 24 hours (Figure 5B), which was presumably formed by the non-oxidative PPP [28]. We did not detect the formation of [M1-^{13}C]-sorbitol in [1,2-^{13}C]-glucose-labelled hepatocytes. We also failed to detect [M1-M5-^{13}C]-sorbitol in hepatocytes labelled with [U-^{13}C]-glutamine.

To characterize the contribution of AR deletion to the phenotype more in depth, we analyzed the urine from age-matched WT, TALKO, ARKO, and DKO mice. As shown in Figure 5C, a dramatic accumulation of polyols was detected in TALKO mice over WT controls, ranging from 1.6-fold for sorbitol to 7.2-fold for C5-polyol, 9.7-fold for sedoheptitol, and 216-fold for erythritol. The build-up of each of these polyols was abrogated by the inactivation of AR

in DKO mice (Figure 5C). Of note, the accumulation of erythritol, ribitol, and sedoheptitol is directly attributed to the enzymatic activity of AR (Extended Data Figure 1E).

Moreover, urine analyses provided evidence for increased oxidative stress on the organismal level by detecting consistent accumulation of established biomarkers, such as lipid hydroperoxides (4-hydroperoxy-2-nonenal, 4-oxo-2-nonenal, and 4-peroxy-2-nonenal) [33], oxidized DNA (8-oxoguanine and 8-oxo-2-deoxyguanosine) [34], ophthalmic acid [35], and homocysteine [36] in TALKO mice, all of which were normalized upon AR inactivation in DKO mice (Figure 5D). Utilizing area under the receiver operating characteristic curve (AUC) logistic regression approach of Metaboanalyst 5.0, we ranked the urinary oxidative stress biomarkers that effectively discriminated TALKO from WT samples (8-oxoguanine: AUC=1, p=0.006; 4-hydroxy-2-nonenal: AUC=0.95; p=0.001; homocysteine: AUC=0.95, p=0.005; 4-hydroperoxy-2-nonenal: AUC=0.95, p=0.006; 8-oxo-2-deoxyguanosine: AUC=0.825, p=0.023; ophthalmic acid: AUC=0.775; p=0.072). These biomarkers indicate that oxidative stress modified DNA and lipid membranes, which potentially mediate the documented changes in gene expression and cellular injury. Uric acid levels were also elevated in the urine of TALKO mice but reversed in DKO mice (Figure 5D). With regards to medical relevance, high urinary uric acid levels have been linked to the recurrence of HCC in human subjects [37].

Sorbitol is an established inducer of mitochondrial ROS production and JNK pathway activation [21], which are involved in hepatocarcinogenesis in TAL deficiency [11]. Therefore, we evaluated whether sorbitol could stimulate the proliferation of 1875 hepatoma cells newly established from the liver of a TALKO mouse. First, we confirmed that [M6-^{13}C]-sorbitol was taken up by TALKO hepatoma cells. We also found that sorbitol was metabolized into [M5-^{13}C]-C5-polyol, [M2-^{13}C]-6PG, [M6-^{13}C]-O8P, and [M4-^{13}C]-S7P (Figure 5E). Moreover, sorbitol stimulated mitochondrial ROI production (Figure 5F), JNK phosphorylation (Figure 5G) and the proliferation of TALKO hepatoma cells (Figure 5H). These findings suggest that AR inactivation-mediated blockade of hepatocarcinogenesis in TAL deficiency involves a unique combination of reversing NADPH depletion and polyol accumulation.

AR normalizes mitochondrial respiration of TALKO hepatocytes

To delineate the source of oxidative stress within mitochondria, we measured the functional capacity of the ETC. State-3 and state-4 respiration were increased through complexes I, II, and IV while respiratory control ratios (state-3/state-4 respiration) remained unchanged, indicating greater functional capacity and integrity of mitochondria in TALKO mice (Figure 6A). Upon inactivation of AR, state-3 respiration through complex I was normalized, while it remained elevated through complexes II and IV in DKO mice (Figure 6A). Because complex I is a primary source of oxidative stress [38], we assessed ROI production and mitochondrial transmembrane potential ($\Delta\Psi m$) by flow cytometry (Supplementary Figure 7) [10]. Elevation of $\Delta\Psi m$ or mitochondrial hyperpolarization (MHP) in TALKO hepatocytes was detected by increased JC1/MTG ratio (Figure 6B). MHP is a result of accumulation of electrons on the inner mitochondrial membrane that facilitates their transfer onto molecular oxygen, thus resulting in the formation of O_2^- [39]. Such elevated production of ROI in

TALKO mice was detected by increased HE and DHR fluorescence over mitochondrial mass measured by MTG fluorescence; Figure 6B). Importantly, augmented MHP and ROI production of TALKO mice were reversed in DKO mice, identifying AR as a regulatory checkpoint of mitochondrial ROI production (Figure 6B), a critical trigger of hepatocarcinogenesis. Intramitochondrial GSH was only reduced in TALKO mice (MCB; Figure 6C). Thus, mitochondria of TAL-deficient livers exhibited MHP, increased ROI production and GSH depletion, each of which was completely reversed by inactivation of AR. However, mitochondrial mass was increased in isolated hepatocytes of both TALKO (4.2±0.9-fold, p=0.0045) and DKO mice (5.5±0.5-fold, $p=3.7\times10^{-6}$) (Figure 6D).

TALKO hepatocytes exhibited greater oxygen consumptions rates (OCR), baseline and maximal mitochondrial respiration, and ATP production (Figure 6E) in accordance with MHP and increased ETC activity of isolated mitochondria (Figure 6A and B). Despite increased mitochondrial ETC capacity and *in vitro* ATP synthesis, intracellular ATP levels were diminished in TALKO mice and, to a lesser extent, in ARKO and DKO mice (Figure 6G). Such differences between increased mitochondrial capacity to produce ATP *ex vivo* (Figure 6E) and diminished ATP levels and reduced adenylate energy charge (AEC) [40] in freshly isolated livers (Figure 6H) indicated a role for the TAL-AR axis in restraining mitochondrial function and redirecting metabolic fluxes towards the cytosol (Figure 6I). Given that most cancer cells generate ATP through aerobic glycolysis rather than oxidative phosphorylation, which has been termed “the Warburg effect” [41], we examined whether such metabolic shift occurred in TALKO mice. Baseline extracellular acidification rate (ECAR) was higher in TALKO and DKO hepatocytes relative to WT and AR controls, respectively (Figure 6F). Moreover, glycolysis and glycolytic capacity were greater in DKO relative to ARKO hepatocytes (Figure 6F). Neither AR inactivation that restored NADPH levels (Figure 6G), nor NAC treatment that restored GSH levels and OCR (Supplementary Figure 8A), corrected enhanced ECAR or glycolytic capacity of TALKO hepatocytes (Supplementary Figure 8B). However, both of these interventions blocked mitochondrial ROI production and carcinogenesis. Therefore, mitochondrial oxidative stress rather than ‘the Warburg effect” is the metabolic driver of hepatocarcinogenesis in TAL deficiency. Furthermore, AR inhibitors, zopolrestat and sorbinil, blocked the serum replenishment-induced proliferation of HepG2 hepatoma and MCF7 breast cancer cell lines *in vitro,* suggesting that pharmacological AR blockade may have utility for treatment of HCC (Extended Data Figure 5).

The TAL-AR axis controls metabolic flux between the PPP and TCA cycle

Although the primary source of NADPH in mammalian cells is the PPP [2], it can be also generated from oxidation of glutamate, isocitrate, and malate by glutamate dehydrogenase (GDH) , isocitrate dehydrogenase (IDH), and malic enzyme (ME), respectively [28]. These TCA cycle substrates shuttle between mitochondria and the cytosol and transport reducing power (Figure 6I). While glutamate and malate were progressively depleted in TALKO and DKO mice, isocitrate was strikingly normalized in DKO mice (Figure 6G). Along these lines, mitochondrial IDH2 but not cytosolic IDH1 was overexpressed in TALKO and DKO mice (Extended Data Figure 3B). Following siRNA-mediated knockdown of IDH2, NADPH/NADP ratio was increased in 1875 TALKO HCC cells (Figure 7A). As

expected, following IDH2 knockdown, [M4-^{13}C]-citrate was accumulated in TALKO HCC cells labelled with [U-^{13}C]-glutamine (Figure 7B) or [1,2-^{13}C]-glucose (Figure 7C). The % labeling of M4 citrate was increased over that of M5 citrate, suggesting that the TCA cycle primarily operated in the forward direction involving oxidative decarboxylation [42]. However, the knockdown of IDH2 further increased the enrichment of M4-citrate and further reduced the enrichment of M5-citrate, suggesting that IDH2 tilted carbon flux into the reverse direction in [U-^{13}C]-glutamine-labelled TALKO hepatocytes (ANOVA p=0.0087; Figure 7B) [42]. This finding is consistent with the accumulation of NADPH upon IDH2 knockdown in TALKO hepatocytes (Figure 7A). Therefore, the selective normalization of isocitrate may tilt the activity of IDH2 into the forward reaction of the TCA cycle resulting in greater intra-mitochondrial NADPH/NADP ratio and correction of mitochondrial ROI levels in DKO mice.

The accumulation of [M1-^{13}C]-S7P, [M2-^{13}C]-S7P, [M3-^{13}C]-S7P, [M4-^{13}C]-S7P, [M5-^{13}C]-S7P, and [M6-^{13}C]-S7P was markedly enhanced in [1,2-^{13}C]-glucose-labelled TALKO hepatoma cells treated with IDH2 siRNA (Figure 7C), demonstrating that IDH2 reduced carbon sequestration in the non-oxidative PPP upon inactivation of TAL. The enrichment of [M1-^{13}C]-G6P and [M2-^{13}C]-G6P was not affected in [1,2-^{13}C]-glucose-labelled TALKO hepatoma cells by IDH2 knockdown (Figure 7C). However, IDH2 knockdown increased the accumulation of [M2-^{13}C]-sedoheptitol and [M2-^{13}C]-C5-polyols in TALKO hepatoma cells (Figure 7D), indicating the interconnectivity of the TCA cycle and the non-oxidative PPP.

Similar to TALKO hepatoma cells (Figure 7), IDH2 knockdown increased the enrichment of [M4-^{13}C]-citrate in WT primary hepatocytes labelled with [U-^{13}C]-glutamine (Extended Data Figure 6A). In contrast, IDH2 knockdown reduced the enrichment of [M4-^{13}C]-citrate in DKO primary hepatocytes labelled with [U-^{13}C]-glutamine (Extended Data Figure 6A, ANOVA p=0.0065). Crosstalk between the non-oxidative PPP and TCA was also substantiated by the considerable accumulation of [M2-^{13}C]-citrate following IDH2 knockdown in primary hepatocytes labelled with [1,2-^{13}C]-glucose (Extended Data Figure 6B). In [1,2-^{13}C]-glucose-labelled hepatocytes, dual TAL and AR inactivation altered carbon flux through the TCA, as evidenced by greater accumulation of [M1-^{13}C]-citrate and [M2-^{13}C]-citrate in DKO mice (Extended Data Figure 6B). Thus, AR inactivation enhanced carbon flux from the non-oxidative PPP towards the TCA cycle in DKO mice. IDH2 knockdown in primary hepatocytes labelled with [1,2-^{13}C]-glucose selectively stimulated the enrichment of [M2-^{13}C]-citrate in WT mice and of [M1-^{13}C]-citrate in DKO mice (Extended Data Figure 6B). Collectively, these isotope labeling studies indicate that the TAL-AR axis impacts carbon flux through the TCA cycle.

IDH2 knockdown markedly enhanced the accumulation of [M1-^{13}C]-S7P and [M2-^{13}C]-S7P in [1,2-^{13}C]-glucose-labelled DKO hepatocytes, suggesting that IDH2 activity mitigated carbon sequestration in the non-oxidative PPP caused by inactivation of the TAL-AR axis (Extended Data Figure 7A). The formation of [M5-^{13}C]-O8P and [M6-^{13}C]-O8P was surprisingly diminished in TALKO and DKO hepatocytes labelled with [1,2-^{13}C]-glucose (Extended Data Figure 7B). Thus, S7P and O8P fluxes were shifted into strikingly opposite

directions by in TALKO and DKO hepatocytes (Extended Data Figure 7A and B), indicating that the TAL-AR axis promotes carbon flux from S7P to O8P.

In primary hepatocytes labelled with [1, 2-^{13}C]-glucose, the enrichment of [M1-^{13}C]-R5P and [M2-^{13}C]-R5P were enhanced in TALKO mice. Similar to hepatoma cells, the enrichment of [M1-^{13}C]-G6P and [M2-^{13}C]-G6P was not affected in [1,2-^{13}C]-glucose-labelled primary hepatocytes by TAL or AR inactivation (Extended Data Figure 7C). [M2-^{13}C]-erythronic acid was enriched in TALKO hepatocytes labelled with [1,2-^{13}C]-glucose (Extended Data Figure 7D). The accumulation of erythronic acid is a key feature of TAL deficiency in humans and mice [43]. The accumulation of [M2-^{13}C]-erythronic acid in TAL deficiency was moderated by IDH2 knockdown. Interestingly, [M2-^{13}C]-erythronic acid also accumulated in ARKO and DKO mice, but it remained unaffected by IDH2 knockdown (Extended Data Figure 7D).

DISCUSSION

The present study reveals that disease progression from cirrhosis to HCC and acetaminophen-induced liver necrosis are critically dependent on NADPH depletion and polyol production by AR, while this enzyme protects from carbon trapping in the PPP and stunted growth in TAL deficiency. The TAL-AR axis distorts carbon sequestration and NADPH production by the PPP into opposite directions. AR inactivation aggravates the accumulation of S7P in TAL deficiency, suggesting that directionality of AR on metabolic flux within the PPP depends on activity of TAL. These results thus advocate for the reformulation of the PPP to include AR as a rheostat of carbon recycling and NADPH output (Figure 6I and Extended Data Figure 1F). Both TAL and AR are confined to the cytosol, however, their inactivation also impacts mitochondrial function characterized by the elevation of $\Delta\Psi m$ or MHP, ETC activity, mitochondrial ROI production, and metabolic flux through the TCA cycle. Beyond promoting S7P accumulation, AR inactivation enhanced carbon flux from the non-oxidative PPP towards the TCA cycle. Alternatively, the knockdown of mitochondrial TCA enzyme, IDH2, further stimulated the accumulation of S7P in hepatocytes of DKO mice. These findings demonstrate the directionality of the TAL-AR axis and its interconnectivity with the TCA cycle, which have broad implications for metabolic reprogramming of body weight and disease progression from cirrhosis to HCC.

Our study shows that carbon sequestration in the PPP leads to a deficiency of substrates for the TCA cycle and amino acid production. Most tissues other than visceral fat have a single set point for mass control as a function of body size [44]. In support of weight gain, glucose and lipid homeostasis have adjustable set points, while amino acid and nucleotide metabolism appear to have single set points; accordingly, the former are vulnerable to homeostatic dysregulation while the latter are not [44]. However, this model of body size control may require revision from the perspective of the PPP as it operates with or without TAL. As shown by this study, TAL is required for efficient carbon recycling through the PPP, and the absence of this enzyme markedly limits the ability of the liver to synthesize amino acids, lipids, and nucleotides. Moreover, the inactivation of AR independently limits the recycling of sugars, such as erythrose, and restricts body size alone.

The sequestration of carbon in non-oxidative PPP substrates elicited the depletion of amino acids (glutamine, alanine, valine, leucine/isoleucine, aspartate, and serine; Extended Data Figure 2B). Depletion in these amino acids, especially branched chain amino acids (valine, leucine/isoleucine), are significant metabolic predictors of body size [45]. While diminished body size in TAL-deficient mice was predictable given a similar growth retardation in children [14], the reduced weight of AR-deficient mice and the synergistic restriction by TAL and AR on weight gain were both surprising and dramatic (Figure 2A). The overall limitation of body size by inactivation of the TAL-AR axis suggests that these two enzymes bestow robustness to metabolic circuits, thereby balancing growth and development within a reducing environment.

In support of carbon sequestration in the PPP by TAL deficiency, labeling of primary hepatocyte cultures with [1,2-^{13}C]-glucose indicated a greater enrichment of [M1-^{13}C]-S7P and [M2-^{13}C]-S7P in the absence of TAL in comparison to WT hepatocytes. The extent of [M1-^{13}C]-S7P exceeded that of [M2-^{13}C]-S7P, suggesting a greater blockade of carbon flux through the oxidative branch of the PPP. Moreover, labeling of primary hepatocyte cultures with [U-^{13}C]-glutamine showed a greater accumulation of [M1-^{13}C]-S7P and [M1-^{13}C]-R5P in the absence of TAL, indicating that sequestration of carbon in the PPP syphons off metabolites from the TCA cycle. Inclusion of AR in the PPP is also supported by isotope tracing studies. In primary hepatocytes labelled with [1,2-^{13}C]-glucose, the inactivation of AR promoted a robust accumulation of [M1-^{13}C]-R5P, which is formed by the oxidative PPP [28]. AR inactivation also led to a 26-fold accumulation of [M2-^{13}C]-erythronic acid, a key feature of TAL deficiency in humans and mice [43]. Moreover, a mechanistic role for AR in the PPP is supported by its direct metabolism of erythrose, ribose, and sedoheptulose. Dual TAL and AR inactivation altered carbon flux through the TCA, as evidenced by greater accumulation of [M1-^{13}C]-citrate and [M2-^{13}C]-citrate in [1,2-^{13}C]-glucose-labelled hepatocytes from DKO mice. The reversibility of TCA flux, in particular NADPH synthesis by IDH2, may underlie reduced mitochondrial oxidative stress and elevated ATP production in DKO mice. Collectively, these isotope labeling studies indicate that the TAL-AR axis modulates carbon flux between the PPP and the TCA cycle.

Tracing NADPH production with deuterated [3-^{2}H]-glucose through the oxidative PPP unveiled diminished enrichment of ^{2}H-NADPH and ^{2}H-NADPH/^{2}H-NADP ratio, which is consistent with reduced transfer of labeled hydride from 6-PG onto $NADP^+$ [28] in TALKO hepatocytes. In accordance with the overall correction of NADPH levels, inactivation of AR restored the enrichment of ^{2}H-NADPH in DKO hepatocytes labelled with [3-^{2}H]-glucose.

The results also show that the TAL-AR axis distorts the NADPH/NADP and the GSH/GSSG ratio into opposite directions. Interestingly, changes in GSH and GSH/GSSG ratio followed different patterns between TALKO and DKO mice. Of the total GSH pool, oxidized GSH (GSSG) normally represents 0.1%−1% of the total glutathione (GSH+GSSG) content [46]. To maintain the GSH/GSSG Nernst potential in the setting of oxidative stress, cells regenerate GSH at the expense of NADPH by the enzyme GSH reductase, synthesize GSH de novo, or extrude GSSG from the cell [47]. The ability to export GSSG is an important factor in mitigating oxidative stress [48]. Since GSH remained depleted while NADPH was corrected in DKO mice, we tested the hypothesis that AR influenced *de novo* GSH synthesis. Among

the genes involved in GSH metabolism, the expression of QPCT, which catalyzes the formation PGA[31], was diminished on the RNA and protein levels in TALKO and DKO livers. PGA was depleted in TALKO and DKO mice, but it was accumulated in ARKO mice. PGA is an intermediate in the recycling of glutamate, which is a precursor of GSH. PGA accumulates when *de novo* synthesis of GSH is inhibited [32]. In support of this mechanism of control over GSH synthesis, PGA was directly metabolized by AR *in vitro,* and it was accumulated in ARKO mice *in vivo*. Moreover, AR inactivation caused the accumulation of [M1-^{13}C]-PGA and [M2-^{13}C]-PGA, and it reduced *de novo* synthesis of [M5-^{13}C]-GSH in [U-^{13}C]-glutamine-labelled hepatocytes. These results indicate that AR itself promotes *de novo* GSH synthesis via the recycling of PGA. Therefore, AR inactivation is mechanistically responsible both for the reversal of NADPH depletion and the persistence of GSH depletion in DKO mice. APAP damages hepatocytes via production of N-acetyl-para-benzoquinone imine, which can be neutralized by conjugation with GSH [17] or reduced back to acetaminophen by NADPH [18]. Our results thus demonstrate NADPH rather than GSH controls the detoxification of acetaminophen in DKO mice. NADPH-dependent formation of polyols was also moderated by AR inactivation.

Polyols exert osmotic toxicity to hepatocytes [20] and other cells [21]. Among polyols, sorbitol, C5-polyols, sedoheptitol, and erythritol were strikingly accumulated in the urine of TALKO mice, which were also characteristic for human subjects with TAL deficiency [14]. Polyol accumulation was also noted recently in patients with HCC in the setting of TAL deficiency [12, 13]. The buildup of each of these polyols was abrogated by the inactivation of AR in DKO mice. In accordance with its NADPH-sparing effect, the deletion of AR markedly reduced the accumulation of metabolites reflecting oxidative stress, such as lipid hydroperoxides, oxidized DNA, ophthalmic acid, and homocysteine in the urine of DKO over TALKO mice. Uric acid levels were also elevated in the urine of TALKO mice but reversed in DKO mice. Of note, high urinary uric acid levels have been linked to recurrence of HCC in human subjects [37]. Moreover, sorbitol stimulated mitochondrial ROI production, proliferation, and JNK phosphorylation in TALKO hepatoma cells. Most studies addressing osmotic stress employ sorbitol at 400–500 mM concentrations [21]. However, we also tested lower concentrations and noted that 25–50 mM sorbitol induced mitochondrial oxidative stress, JNK activation, and hepatocyte proliferation, which are likely to have biological relevance. These findings provide evidence that the blockade of hepatocarcinogenesis by AR inactivation may involve a simultaneous reversal of NADPH depletion and polyol accumulation in TAL deficiency. While the restoration of NADPH and the reversal of polyol accumulation are *direct* consequences of AR deletion, the abrogation of oxidative stress and further buildup of metabolites of the non-oxidative branch of the PPP may be considered *indirect* metabolic consequences of AR deletion in DKO mice.

Mitochondrial oxidative stress in TALKO hepatocytes was evidenced by measurements of elevated $\Delta\Psi m$ or MHP and increased ROI production. MHP is a result of accumulation of electrons on the inner mitochondrial membrane that facilitates their transfer onto molecular oxygen, thus resulting in the formation of O_2^- [39]. Importantly, augmented MHP and ROI production of TALKO mice were reversed in DKO mice, identifying AR as a regulatory checkpoint of mitochondrial ROI production, a critical trigger of hepatocarcinogenesis. In accordance with their established roles in mitochondrial oxidative stress, expression of

NDUFS3 [29], Bak1 [51], and NQO1 [30] was increased on the RNA and protein levels in TALKO livers. Each of these genetic checkpoints of oxidative stress along with reduced NADPH/NADP ratio were reversed by inactivation of AR in DKO hepatocytes. Gene expression and siRNA-mediated knockdown studies implicated IDH2 in mitochondrial oxidative stress of TALKO mice. Consistent with a permissive role for IDH2 in mitochondrial oxidative stress, the NADPH/NADP ratio was increased by IDH2 knockdown in TALKO HCC cells. Crosstalk between the non-oxidative PPP and TCA was corroborated by the accumulation of S7P in primary hepatocytes labelled with [U-^{13}C]-glutamine or [1,2-^{13}C]-glucose. IDH2 knockdown enhanced the accumulation of [M1-^{13}C]-S7P, [M2-^{13}C]-S7P, [M4-^{13}C]-S7P, [M5-^{13}C]-S7P, [M6-^{13}C]-S7P in [1,2-^{13}C]-glucose-labelled DKO hepatocytes, indicating that IDH2 activity mitigated carbon sequestration in the non-oxidative PPP upon inactivation of the TAL-AR axis. Although NADPH production by the oxidative PPP is known to influence mitochondrial respiratory activity in yeast [52], the impact of the non-oxidative PPP on mitochondrial respiration has not been documented. These studies thus provide previously unknown mechanistic evidence that the mitochondrial TCA cycle is connected to carbon sequestration in the non-oxidative PPP upon inactivation of the TAL-AR axis.

O8P has been earlier proposed as a substrate of the PPP by using crystalized transketolase and TAL from yeast [53] and by metabolite analysis of rat livers [54]. Recent reviews have not included O8P in the PPP [2, 55]. However, our isotope labeling studies of primary hepatocytes with [1,2-^{13}C]-glucose provided evidence for the formation of [M5-^{13}C]-O8P and [M6-^{13}C]-O8P, which was profoundly diminished in the absence of TAL, clearly showing the involvement of O8P in the PPP. Formation of [M5-^{13}C]-O8P and [M6-^{13}C]-O8P was also reduced in DKO hepatocytes. These findings support the notion that O8P is a metabolite of the PPP (Extended Data Figure 1F), with new evidence that that the TAL-AR axis promotes carbon flux from S7P to O8P within the non-oxidative PPP. An analogous mechanism is implied by robust accumulation of O8P and marked depletion of S7P in *Leishmania* lacking transketolase [56].

TAL deficiency predisposes to cirrhosis, HCC, and APAP-induced liver failure in mice [11] and human subjects [12–14, 16, 26]. Notably, frequencies of HCC and liver cell dysplasia were also increased in mice with TAL haplo-insufficiency [11]. TAL haplo-insufficiency is more common among patients with APAP-induced liver failure as compared to normal blood donors [16, 26]. The present study suggests that AR inhibitors may potentially protect from HCC and APAP toxicity in subjects with TAL deficiency.

Besides TAL deficiency, AR expression is elevated in up to 95% of human cases of HCC [22]. Overexpression of AR is also detectable in patients with lung [57] and breast cancer [58]. However, direct evidence for blockade of cancer by inactivation of AR has been lacking. The elimination of cancer in TALKO mice by deleting AR provides a causal insight into hepatocarcinogenesis. Moreover, the results provide a clear, mechanistic rationale for targeting AR for treatment of HCC. Hereby, our data show that AR inhibitors, zopolrestat and sorbinil, block the proliferation of hepatoma and breast cancer cells *in vitro.* Therefore, this study unveils an essential role for AR in a clinically relevant model of hepatocarcinogenesis with implications for diagnosis and treatment of additional common forms of cancer. The ability of AR blockade to inhibit cancer cell proliferation is expected

to depend on the selective involvement of this enzyme in resistance to oxidative stress. While the present study identifies the TAL-AR axis as a regulatory checkpoint between cytosolic aldose metabolism and mitochondrial oxidative stress during hepatocarcinogenesis, it recognizes the complexity of these interactions and the need to further refine the metabolic pathways that connect the PPP and the TCA cycle.

MATERIALS AND METHODS

This research has been conducted in compliance with all institutional policies and annual approval of the Institutional Biosafety and the Institutional Animal Care and Use Committees of Upstate Medical University of the State University of New York.

Mice.

Mice with heterozygous deletion of transaldolase ($TALDO1^{+/-}$) were created and fully backcrossed for >10 generations onto the C57BL/6 strain, as earlier described [10]. $TALDO1^{+/-}$ and *Akr1b3*-deficient aldose reductase (AR) knockout (ARKO) strains [59] were crossed to generate double-knockout (DKO) mice lacking both TAL and AR. Both TAL-deficient and DKO mice were breed as heterozygotes for the TALDO1 locus, as homozygous TAL deficiency causes male infertility due to mitochondrial dysfunction in sperm cells [10]. Wild-type (WT or $TAL^{+/+}AR^{+/+}$), TAL-deficient (TALKO or $TAL^{-/-}AR^{+/+}$), AR-deficient (ARKO or $TAL^{+/+}AR^{-/-}$), and double-deficient (DKO, or $TAL^{-/-}AR^{-/-}$) mice were matched for age and gender in each experiment. Sensitivity to acetyl-p-aminophenol (APAP) was tested as earlier described [11]. Briefly, APAP was dissolved in phosphate buffered saline (PBS) at 70ºC, allowed to cool to 37ºC and then injected intraperitoneally at 800 mg/kg. Prior to APAP injection mice were fasted for food, but not water, overnight [11]. APAP-treated mice were continuously monitored up to 24 hours and euthanized at the earliest sign of distress. N-acetylcysteine (NAC) was provided to mice at 10 g/l in drinking water throughout their life, including treatment of their parents, as earlier described [10, 11]. Animal experimentation has been approved by the Committee on the Human Use of Animals in accordance with NIH Guide for the Care and Use of Laboratory Animals.

Liver histology.

At the time of sacrifice, liver was removed from each mouse, cut into ~ 5 mm diameter blocks, and transferred into 10% formalin. Samples were paraffin-embedded, sectioned, and visualized with hematoxylin-eosin or Gömöri-trichrome staining. Images were taken with an Olympus CX43RF microscopy equipped with a DP-22 CCD color camera using C ellSense Software.

Slides were scored independently by expert pathologists blinded to genetic background or treatment groups. Although the morphology of HCC is usually quite heterogeneous in human subjects, the most widely used scoring system is based on the Edmonson 4-grade scale [60] and recommendations of the International Consensus Group for Hepatocellular Neoplasia [61]. There is considerable heterogeneity in disease progression in mouse models of HCC which is largely dependent on the underlying pathogenesis, such as induction by chemicals, diet, or genetic intervention. In TALKO mice 4 stages of hepatocarcinogenesis

were delineated which were characterized by 1) anisonucleosis; 2) anisonucleosis with increased mitotic figures; and 3) anisonucleosis with dysplastic nodules as pre HCC stages; and 4): HCC with macroscopically visible tumor and histological evidence for invasion of normal tissue by pleomorphic and often anaplastic giant hepatocytes [61].

Isolation of mitochondria.

Liver mitochondria were isolated by differential centrifugation as previously described [29]. Livers were removed, cut into small pieces which were mechanically disrupted in a 15-ml Dounce homogenizer on ice in liver mitochondria isolation medium (LMIM) containing 250mM sucrose, 10mM Tris, 1mM EGTA, pH 7.4. Homogenate was centrifuged at 1,000 x g for 3 minutes at 4°C. The supernatant was transferred to new tubes and then centrifuged at 10,000 x g for 10 minutes at 4°C. The pellet was resuspended in LMIM and centrifuged again at 10,000 x g for 10 minutes at 4°C. The mitochondrial pellet was then resuspended in a Ca^{2+} chelating buffer containing 195 mM mannitol, 25 mM sucrose, 40 mM HEPES pH 7.2, 1 mM EGTA, 10 mM NaCl, and 5 mM succinate at room temperature. This mitochondrial solution was homogenized in a 2-ml Dounce homogenizer and then stirred at room temperature for 10 minutes and then on ice for 5 minutes. Mitochondria were centrifuged at 10,000 x g for 10 minutes at 4°C and resuspended in liver swelling buffer (LSB), which contained 195 mM mannitol, 25 mM sucrose, 40 mM HEPES pH 7.2 at 4°C. Mitochondria were centrifuged at 10,000 x g for 10 minutes at 4ºC twice and then resuspended in 1 mL of LSB and protein content was measured by Bradford assay. Mitochondria were kept on ice for 1 hour before using in downstream analyses. NaCl, 4-(2-hydroxyethyl)-1-piperazineethanesulfonic acid (HEPES), sucrose, and ethylene glycol-bis(2-aminoethylether)-N,N,N′,N′-tetraacetic acid (EGTA) were obtained from Sigma-Aldrich (St. Louis, MO). Tris-HCl was obtained from USB (Cleveland, OH). Succinic acid was obtained from Acros Organics (Geel, Belgium).

Measurement of mitochondrial electron transport chain (ETC) activity.

ETC activity was measured in the absence and presence of substrates specific for individual complexes I, II, and IV using Oxygraph, a Clark-type O_2 electrode (Hansatech, Norfolk, UK), as earlier described [29]. During the assay of each ETC complex, 150 uM ADP and 150 uM Pi were added to attain state-3 respiration; when the ADP has been exhausted state-4 respiration was attained; after achieving a stable rate for state-4 respiration, 2uM mClCCP was added to measure uncoupled O_2 consumption. Maximal ETC capacity was determined by O_2 consumption of uncoupled mitochondria. In contrast, oxidative phosphorylation (OXPHOS), which is a key element of bioenergetics, is measured as maximum ADP-stimulated respiration or state-3 respiration. State-4 is the respiratory state obtained in isolated mitochondria after state-3, when added ADP is phosphorylated completely to ATP driven by electron transfer from defined respiratory substrates to O_2. Conventionally, ADP stimulation is expressed by the respiratory control ratio (RCR = State-3/State-4), which is frequently used as an index of coupling for diagnosis of mitochondrial defects. Briefly, 300 μg of mitochondria at a final protein concentration of 1μg/μl were added to mitochondrial respiration buffer (RB; 300mM mannitol, 10mM KCl, 5mM $MgCl_2 \times 6H_2O$, 5mM KH_2PO_4, pH 7.4) which contained 150 μg of fatty-acid free bovine serum albumin (Catalog No. 03117057001 Roche, Basel, Switzerland) at 37°C in the Oxygraph chamber. To test complex

I activity, we added 5 mM pyruvate (Catalog No. 11840–030, Gibco) and 2.5 mM malate (Catalog No. M7397, Sigma-Aldrich), followed by 150μM adenosine diphosphate (ADP; Catalog No. A5285, Sigma-Aldrich) and 150μM inorganic phosphate (P_i) to measure state 3 and 4 respiration, then 2 μM carbonyl cyanide m-chlorophenylhydrazone (mClCCP; Catalog No. C2759, Sigma-Aldrich) to measure uncoupled mitochondrial respiration. Complex II activity was measured with addition of 10 μM rotenone (Catalog No. 45656, Sigma-Aldrich) to inhibit complex I followed by addition of 2.5 mM succinate (Catalog No. AC20874, Acros-Organics). This was followed by addition of 150 μM ADP and 150μM inorganic phosphate and 2 μM mClCCP as in complex I. Complex IV was measured in the presence of 100 μM antimycin A (Catalog No. A8674, Sigma-Aldrich) to inhibit complex III, then we added 6 mM ascorbate (Catalog No. A5960, Sigma-Aldrich) and 0.2 mM N,N,N′,N′-tetramethyl-p-phenylenediamine (TMPD; Catalog No. T7394, Sigma-Aldrich), which was followed with the addition of ADP, P_i, and mClCCP, as described for complexes I and II. Each measurement was performed in duplicate and their means were used as the result for each experiment.

Isolation of hepatocytes for metabolic studies.

For analysis of metabolic activity within intact hepatocytes, livers were perfused through the portal vein *in situ* [11]. Briefly, mice were sedated and anesthetized with pentobarbital via intraperitoneal injection according to IACUC approved protocols. Hepatocytes were isolated via liver perfusions, as previously described [11]. Media and buffers were filtered through 0.22μM filtration apparatus and brought up to 37°C to prevent collapse of portal vein during perfusion. The abdomen and peritoneum were dissected and the intestines were reflected to allow access to the inferior vena cava and portal vein. Mice were first perfused with 50 mL of Buffer A (HBSS pH 7.4 without calcium or magnesium (Catalog No. 21–022-CM, Corning) plus 0.5 mM EGTA (Catalog No. E4378, Sigma-Aldrich) followed by 50 mL of Buffer B (HBSS pH 7.4 without calcium or magnesium with 1 mM $CaCl_2$ (Catalog No. C7902, Sigma-Aldrich), 15mM HEPES (Catalog No. H4034, Sigma-Aldrich), and 100 U/mL Type 4 collagenase (Catalog No. LS004212, Worthington Biochemical, Lakewood, NJ). Both perfusion buffers were pre-warmed at 37°C. The portal vein was cannulated with a 25-gauge needle and buffer A flow was initiated at a rate of 5 mL/minute. When the liver began to blanch, the inferior vena cava was severed and buffer A was perfused at 10 mL/minute which was followed by perfusion of buffer B at 10mL/minute. The liver was then excised and placed in a Petri dish containing 5mL of buffer B. The capsule was then cut open to allow the release of hepatocytes into solution. Hepatocytes were filtered through a 70 μm filter and washed with isolation medium (high glucose Dulbecco's Modified Eagle Medium (DMEM), L-glutamine free, Na-Pyruvate free (Corning Catalog No. 150–17-CV, with 1% antibiotics (30–004-CI, Corning). Hepatocytes were centrifuged at 50 x g for 3 minutes at 4°C. The pellet was washed and pelleted twice more in isolation medium. Prior to seeding of hepatocytes, XF 96-well culture plates (Catalog No. 101085–004, Seahorse Bioscience, North Billerica, MA) were pre-coated in PBS with 100 μg/ml collagen (50 μl/well) overnight followed by washes in adherence medium [11]. Cells were plated at 10,000 cells/well in adherence medium (high glucose DMEM, L-glutamine free, Na-Pyruvate free with 1% antibiotics, and 10% fetal bovine serum (Catalog No. 26140079, ThermoFisher) in a collagen-precoated XF 96-well culture plate. After 4 hours, the adherence medium

was removed and replaced with culture medium (high glucose DMEM, L-glutamine free, Na-Pyruvate free with and 1% antibiotics). Cells were cultured overnight on collagen-coated 96-well Seahorse metabolic plates in 5% CO_2 at 37°C for 24 h prior to analysis. Next, the culture medium was removed, and the cells were washed with either liver glycolysis medium (Seahorse XF Base Medium (Catalog No. 102353–100, Seahorse Bioscience), 2mM glutamine,) or mitochondrial stress test medium (Seahorse XF Base Medium, 2mM glutamine, 1mM pyruvate, 25 mM glucose). Cells were then equilibrated with 175 µl of either glycolysis or mitochondrial stress test medium. Hepatocytes were incubated at 37°C in ambient atmosphere for 60 minutes before using a Seahorse XF^e96 Analyzer (North Billerica, MA). For the glycolysis assay, we injected 10 mM glucose, 1 µM oligomycin, and 50 mM 2-deoxyglucose. For the mitochondrial stress test, we injected 1 µM oligomycin, 2 µM carbonyl cyanide-4-(trifluoromethoxy) phenylhydrazone (FCCP), and 500 nM rotenone/antimycin A. Seahorse Metabolic Analyzer data were acquired with the Wave software version 2.6.

Flow cytometry of mitochondria and liver cells.

Production of reactive oxygen intermediates (ROI) was measured by using oxidation-sensitive fluorescent probes 5,6-carboxy-2',7'-dichlorofluorescein-diacetate (DCF-DA), dihydrorhodamine 123 (DHR), and hydroethidine (HE, Molecular Probes, Eugene, OR) as earlier described [11]. Mitochondria or cells were stained in respiration buffer or tissue culture medium with 0.1 uM DHR for 2 min, 1 uM DCF-DA for 15 min, or 1 uM HE for 15 min and samples were analyzed using a Becton Dickinson LSR-II flow cytometer equipped with 4 lasers (UV/355 nm, blue/488 nm, yellow/561 nm, and red/634 nm). Dead cells and debris were excluded from the analysis by electronic gating on forward (FSC) and side scatter (SSC) measurements. While R123, the fluorescent product of DHR oxidation, binds selectively to the inner mitochondrial membrane, ethidium and DCF remain in the cytosol of living cells, thus, allowing measurement of ROI levels in different subcellular compartments. Mitochondrial transmembrane potential ($\Delta\Psi_m$) was estimated by cationic lipophilic dye 5,5 ',6,6′-tetrachloro-1,1 ',3,3 '-tetraethylbenzimidazolocarbocyanine iodide (JC-1; FL2/FL1 ratio), 3,3'-dihexyloxacarbocyanine iodide ($DiOC_6$), and tetramethylrhodamine methyl ester (TMRM) [10]. Carbonyl cyanide m-chlorophenylhydrazone (mClCCP) was used to dissipate $\Delta\Psi_m$ and confirm specificity of staining. Mitochondrial mass was assessed with nonyl-acridine orange (NAO) and MitoTracker Green (MTG). Glutathione was assessed by fluorescence of monochlorobimane (MCB). All fluorescent probes were obtained from ThermoFisher Scientific/Molecular Probes (Eugene, OR). Following in situ liver perfusions, flow cytometry was also performed on isolated hepatocytes sedimented at 50 x g. Flow Cytometry Data were acquired with the FACSDiva software version 6.0. Flow cytometry data were analyzed with FlowJo software version 10.0.

Transfection of primary hepatocytes with siRNA.

Hepatocytes were seeded in 6-well plates (Falcon Cat. No. 353046) pre-coated with 100 µg/ml collagen (Corning, cat. no. 354236) for 24 hours at 4°C. Isolated cells from the liver perfusion were washed by spinning at 150 g for 30 seconds and resuspended in PBS. After the second spin, cells were resuspended in DMEM adherence medium (high glucose DMEM, L-glutamine free, Na-Pyruvate free with 1% antibiotics at a concentration

of 150,000 cells/mL. 300,000 cells were plated into each well in DMEM for 4–6 hours after verification of hepatocyte attachment to the wells. After wells were washed in PBS twice, cells were cultured in DMEM with 10% fetal bovine serum overnight. For stable isotope labeling, TC wells were aspirated of media and washed with PBS twice. The transfection medium comprised of 150 µl of Opti-Mem (ThermoFisher Cat. No. 31985070) and 9 µl of Lipofectamine RNAiMAX (ThermoFisher Scientific Cat# 13778075) containing 3 µl of scrambled siRNA (30 pmol, Origene Cat.No. SR30004) or IDH2 siRNA (30 pmol, rCrCrCrGrUrGrUrGrGrArArGrArGrUrUrCrArArGrCrUrGAA (Origene Cat.No. SR414742C). Following transfections, cell were cultured in high-glucose DMEM medium (ThermoFisher Scientific Cat# 11965118). For glutamine or glucose stable isotope labeling studies, glutamine-free DMEM (Catalog No. 26140079, ThermoFisher) or glucose-free DMEM was used (ThermoFisher Scientific Cat# 11966025), respectively, in combination with stable isotope-labelled substrates. For siRNA-mediated knockdown, cells were cultured for 24, 48, or 72 hours before harvest for western blot assay or LC-MS/MS.

Metabolic flux analyses in primary hepatocytes labelled with stable isotopes.

For metabolic flux analyses, stable isotope-labelled compounds [1,2-^{13}C]- glucose (CLM-504–0.5), [U-^{13}C]-glucose (CLM-1396–0.5), [U-^{13}C]-glutamine (DLM-1150–0.5), [2-^{2}H]-glucose (DLM-1271–0.5), [3-^{2}H]-glucose (DLM-9294-PK), [4-^{2}H]-glucose (CLM-1822-H-0.25) were obtained from Cambridge Isotope Laboratories (Cambridge, MA) and [1-^{2}H]-glucose was obtained from Omicron Biochemicals (South Bend IN, Cat No GLC-034). For stable isotope tracing in hepatocytes, the culture medium was replaced with glucose-free medium supplemented with 10mM ^{13}C-labelled or ^{2}H-labelled glucose or glutamine-free medium supplemented with 2 mM ^{13}C-labelled L-glutamine. Metabolites of stable isotope-labelled compounds were tracked through the mitochondrial tricarboxylic acid (TCA) cycle, glycolysis, and the pentose phosphate pathway (PPP) [28]. Percent enrichment of labelled metabolites was compared between cells cultured with and without stable isotopes.

Metabolome analysis by LC-MS/MS.

For metabolite extraction, liver pieces weighing approximately 100 mg were resuspended in 400 µl of 80% methanol (−80°C) and homogenized using the Power Gen 500 (Fisher Scientific, Waltham, MA). Before freezing, each extract was spiked with 0.0125 mM 5-thio-glucose, an internal standard that does not occur naturally in mammalian tissues, as earlier described [19]. After freezing at −80°C and thawing once, the sample was centrifuged at 13,000 x g for 30 min at 4°C, and 400µl of supernatant was saved. A 2nd 400 µl of 80 % methanol (−80°C) was added to the pellet, the sample was vortexed, centrifuged at 13,000 × g for 30 min at 4°C, and the 2nd 400 µl of supernatant was saved. The two 400-µl supernatants were combined, dried in a SpeedVac (Savant AS160, Farmingdale, NY), and stored −80 °C until analysis. For analysis of pyridine nucleotides, liver pieces weighing approximately 100 mg were resuspended in 400µl of 0.5M KOH with 10 µl of octanol to prevent foaming. After freezing at −80°C and thawing 3 times, the sample was centrifuged at 13,000 × g for 30 min at 4°C, and then samples were neutralized with 80 µl of $KHCO_3$. The sample was centrifuged again at 13,000 × g for 30 min at 4°C and filtered through 0.45µm PVDF filters. 1.47 ml of 100% methanol (−80°C) was added, the sample was vortexed, centrifuged at 13,000 × g for 5 min at 4°C, and the supernatant was

dried in a SpeedVac. Each sample was resuspended in 20 μl of LC/MS grade water, and 10 μl per sample was injected into a 5500 QTRAP, a hybrid triple quadrupole/linear ion trap mass spectrometer, using a quantitative polar metabolomics profiling platform with selected reaction monitoring (SRM) that covers all major metabolic pathways. The platform uses hydrophilic interaction liquid chromatography with positive/negative ion switching to analyze up to 308 metabolites (289 Q1/Q3 transitions) from a single 15-min targeted liquid chromatography–tandem mass spectrometry (LC–MS/MS) acquisition with a 3-ms dwell time and a 1.55-s duty cycle time [62].

Tracing of stable isotope-labeled compounds was performed a Thermo Scientific Vanquish HPLC coupled to a Thermo Scientific Q Exactive hybrid quadrupole-orbitrap MS. The metabolites were separated using a hydrophilic interaction liquid-chromatography (HILIC) method on a Waters Xbridge BEH Amide column (3.5 μm, 2.1 X 100 mm, P/N: 186004860). The Thermo Scientific Q Exactive MS was operated in polarity switching mode throughout the acquisition run to maximize metabolite coverage. The HESI probe parameters were the following in both polarity modes: sheath gas flow rate 30, aux gas flow rate 10, sweep gas flow rate 0, spray voltage 3.60 kV, aux gas heater temp 120 °C, S-lens RF level 55, ion transfer capillary temp 320 °C. In positive mode, the instrument acquired Full Scan spectra with a m/z range of 61–915, while in negative mode, the Full Scan mass range was m/z 70–920. The resolution of the scans was 70000, the AGC target was 3e6, while maximum IT was 200 ms. Mobile phase component A was 10 mM ammonium acetate and 7.5 mM ammonium hydroxide in water with 3 % (v/v) acetonitrile (pH 9.0) while mobile phase component B was 100 % acetonitrile. The 25-minute-long gradient was as follows: 0 minutes, 85 % B; 1.5 minutes, 85% B; 5.5 minutes, 35 % B; 14.5 minutes, 35 % B; 15.0 minutes, 85 % B; 25.0 minutes, 85 % B. The mobile phase flow rate was the following: 0 minutes, 0.150 ml/min; 10.0 minutes, 0.150 ml/min; 10.5 minutes, 0.300 ml/min; 14.5 minutes, 0.300 ml/min; 15.0 minutes, 0.150 ml/min, 25.0 minutes, 0.150 ml/min. The sample injection volume was 5 μL. Mass spectrometry data were collected with the following softwares: Thermo Q Exactive Tune version2.9, Thermo TraceFinder version 4.1, and Thermo Scientific Xcalibur version 4.1. List of unique metabolites detected by a single 15-min targeted LC–MS/MS acquisition with a 3-ms dwell time and a 1.55-s duty cycle time are shown in Supplementary Table 2.

Metabolite and pathway analysis.

Quantitative enrichment analysis of 504 detected metabolites was utilized for pathway analysis employing the web-based MetaboAnalyst 5.0 software. Mice were matched for age and gender and were injected in the same run. The signal stability was assured by normalizing the controls between runs to the sum of all signals between separate runs using Metaboanalyst. To monitor sample recovery, each cell extract was spiked with 0.0125mM 5-thio-glucose, an internal standard that does not occur naturally in mammalian tissues. The measured compounds were also normalized between samples by sum normalization, log transformation and pareto scaling, using Metabolanalyst. The enrichment analysis was based on global analysis of covariance (Ancova). A Google-map style interactive visualization system was utilized for data exploration and creation of a 3-level graphical output: metabolome view, pathway view, and compound view. The ‘metabolome view’

shows all metabolic pathways arranged according to the scores from enrichment analysis (y axis: −log p) and from topology analysis (x axis: impact: number of detected metabolites with significant p value) [63]. The pathway topology analysis used two well-established node centrality measures to estimate node importance: degree centrality and betweenness centrality. Degree centrality depends on the number of links connected to a given node. For directed pathway graphs, there are two types of degrees: in-degree for links came from other nodes, and out-degree for links initiated from the current node. Here, we only considered the out-degree for node importance measure. Upstream nodes are considered to have regulatory roles for the downstream nodes, and not vice versa. The betweenness centrality measures the number of shortest paths going through the node. Since metabolic networks are directed, we used relative-betweenness centrality for a metabolite importance measure based on metabolite topology weighed by relative-betweenness centrality. The degree centrality measures focus more on local connectivity, while the betweenness centrality measures focus more on global network topology. The node importance values calculated from centrality measures were further normalized by the sum of the importance of the pathway. Therefore, the total/maximum importance of each pathway reflects the importance measure of each metabolite node that is actually the percentage relative to the total pathway importance, and the pathway impact value is the cumulative percentage from the matched metabolite nodes. The altered compounds have been grouped and presented together for each pathway.

Metabolite concentrations were evaluated for their ability to discriminate between wild-type (WT), TALKO, ARKO, and DKO by partial least squares-discriminant analysis (PLS-DA) using MetaboAnalyst. PLS-DA is a supervised method that uses a multi-variate regression technique to extract via linear combination of metabolites (X) the information that can predict the subject group membership (Y). PLS-DA was used to test the hypothesis that changes in concentrations of a group of compounds are capable of discriminating the metabolome of TALKO, ARKO, DKO mice from WT mice. While the unsupervised nature of the principal component analysis algorithm provides unbiased dimensionality, it may only reveal group structure when within-group variation is sufficiently less than between-group variation. In contrast, supervised forms of discriminant analysis such as Partial Least Squares rely on group assignment of each observation which is more sensitive for identifying metabolic differences between groups that have been genetically well defined. The classification and cross validation were performed using the wrapper function offered by the caret package in MetaboAnalyst software. In order to assess that the class discrimination is statistically significant, a permutation test was performed. In each permutation, a PLS-DA model was built between the data (X) and the permuted class labels (Y) using the optimal number of components determined by cross validation for the model based on the original class assignment. The ratio of the between sum of the squares and the within sum of squares (B/W-ratio) for the class assignment prediction of each model was calculated. PLS-DA models were validated by permutation test p value <0.05. Contribution of individual metabolites to PLS-DA was assessed by variable importance in projection (VIP) and coefficient scores. Individual compounds were also compared between WT, TALKO, ARKO, and DKO by paired or unpaired t-test with Welch's correction using Prism software (GraphPad, San Diego, CA). Adenylate energy charge (AEC) has been

calculated according to the Atkinson formula: adenylate energy charge (AEC) = ([ATP] + 0.5[ADP])/([ATP] + [ADP] + [AMP])) [40].

RNA sequencing.

RNA was extracted from livers using the Qiagen miRNeasy kit (Qiagen, Hilden, Germany). RNA quality and quantity were determined using the RNA 6000 Nano Kit on the Agilent 2100 Bioanalyzer (Agilent, Santa Clara, CA). Sequencing library preparation was done with the Illumina TruSeq Stranded Total RNA with RiboZero Gold kit (Illumina, San Diego, CA). Sequencing libraries were quantified using the KAPA Library Quantification Complete Kit Universal (KAPA Biosystems, Wilmington, MA). The pooled library (1.4pM) was loaded onto the NextSeq 500 instrument, using the NextSeq 500/550 High Output v2 Kit for 75 cycles (Illumina, San Diego, CA). RNA-Seq data have been securely transferred, stored, and analyzed in the Illumina BaseSpace Sequence Hub. All RNA-sequencing data have been uploaded to the NCBI Gene Expression Omnibus (Accession GSE217133). RNA Express software was used to assign aligned reads to genes and perform differential gene expression analysis. Cufflinks software was used to profile gene expression and to detect transcript isoforms. Leveraging KEGG, Ingenuity, and Panther GeneOntology databases, integrated analysis of individually matched metabolome and RNAseq results was carried out with MetaboAnalyst. Changes between genotypes at false discovery rate (FDR) p value < 0.05 were further evaluated by western blot.

Western blot analyses.

Liver protein lysates were prepared by sonication in 300 μl of lysis buffer (20mM Tris-HCl, 150mM NaCl, 1mM Na2EDTA, 1mM EGTA, 1% Triton, 2.5mM sodium pyrophosphate, 1mM β-glycerophosphate, 1mM Na3VO4, 1μg/mL leupeptin, 1mM phenylmethanesulfonyl fluoride. Mitochondria were directly dissolved in lysis buffer (20mM Tris-HCl, 150mM NaCl, 1mM Na_2EDTA, 1mM EGTA, 1% Triton, 2.5mM sodium pyrophosphate, 1mM β-glycerophosphate, 1mM Na_3VO_4, 1μg/mL leupeptin; catalog no. 9803, Cell Signaling Technology, Danvers, MA) with 1mM phenylmethanesulfonyl fluoride (PMSF) (catalog no. P7626, Sigma-Aldrich). 40 μg of protein lysates, unless otherwise indicated, were resuspended in Laemmli buffer (20% glycerol, 125mM Tris-HCl, 4% sodium dodecyl sulfate, 10% β-mercaptoethanol, 0.075% bromophenol blue), separated in a 12% SDS-polyacrylamide gel electrophoreses (SDS-PAGE), and electroblotted to nitrocellulose. TAL was detected with rabbit antibody 170 [11]. Aldose reductase (AR) was detected with 5A11A7/H9 mouse IgG2b/kappa hybridoma antibody developed in-house. Rabbit polyclonal Drp1, AMPK, and phospho-AMPK antibodies were obtained from Santa Cruz Biotechnology (Santa Cruz, CA). Rabbit monoclonal antibodies to 4E-BP1 and phospho-4E-BP1 were purchased from Cell Signaling (Danvers, MA). Rabbit monoclonal Rab4A, NDUFS3, OXPHOS cocktail including ATP5A, UQCRC2, MTCO1, SDHB, and NDUFB8 antibodies, rabbit polyclonal GPI1, ME1, PON1, Albumin, and PLTP antibodies were obtained from Abcam (Cambridge, UK). SQSTM1/p62 antibody was obtained from Abnova (Taipei, Taiwan). β-catenin antibody was obtained from BD (Franklin Lakes, NJ). VDAC1 was detected with rabbit monoclonal antibody ab34726 (Abcam, Waltham, MA). Bak1 was detected with rabbit polyclonal antibody sc832 (Santa Cruz). Rabbit monoclonal c-jun (Catalog No. 9165) and pJNK antibodies (Catalog No. 4668) were purchased

from Cell Signaling Technology. Rabbit monoclonal Rab4A (Catalog No. ab108974), NDUFS3 (Catalog No. ab14711), SDHA (Catalog No. 14715), mitochondrial cytochrome c oxidase subunit 1 (MTCO1) of complex IV (Catalog No. 14705), and complex I immunocapture antibody (Catalog No. ab109798) were obtained from Abcam (Cambridge, UK). Apolipoprotein-H antibody (Catalog No. AF6575) was purchased from R&D Systems (Minneapolis, MN). β-actin antibody (Catalog No. Mab1501R) was purchased from Millipore (Billerica, MA). Tubulin rabbit monoclonal antibody (Catalogue No. 2128L) was obtained from Cell Signaling Technology (Danvers, MA). Secondary HRP-conjugated goat anti-mouse antibody (Cat. No. 115–035-146) and goat anti-rat antibody (Cat No.112–005-003) were obtained from Jackson ImmunoResearch Laboratories (West Grove, PA). HRP-conjugated goat anti-rabbit antibody (Cat.No. 7074) was obtained from Cell Signaling Technologies (Danvers, MA). Primary antibodies were employed at 1000-fold dilutions with the exception of β-actin antibody which was employed at 5000-fold dilution. Secondary antibodies conjugated to horse radish peroxidase (HRP) were employed at 1:20000 dilution.

Production and enzymatic activity of recombinant aldose reductase (AR).

Recombinant AR was expressed as a fusion protein with glutathione-S-transferase (GST). AR was affinity purified through binding of its fusion partner, GST, to GSH-agarose beads. Then AR was cleaved from GST with thrombin and detected by a monoclonal antibody to AR via western blotting. Glyceraldehyde (GAD) was used as a positive control for testing of AR activity. Enzyme activity units were calculated based on the ΔOD at 340nm over 60 minutes during which NADPH was depleted [64].

Measurement of cell proliferation.

2,500 cells were seeded for 24 hours in 96-well plates. After washing the wells twice with PBS, fresh medium was added to each well with or without (control) sorbitol for 4, 8, 12, 24, or 48 more hours and cellular DNA content was measured using the CyQUANT Cell Proliferation Assay (ThermoFisher Cat. No. C7026). CyQUANT was excited at 485 nm and detected at 528 nm using a Biotek Synergy 1 Hybrid Multi-mode Microplate Reader (Biotek Instruments Inc., Winooski, VT). Cell viability was assessed with the MTT assay (Abcam Cat.No. 211091) measuring absorbance at 570 nm with the Synergy 1 plate reader. HepG2 hepatoma (catalogue number HB-8065) and MCF7 breast cancer (catalogue number HTB-22) cell lines were obtained from ATCC (Manassas, VA, USA).

Statistical analysis.

Statistical analyses were performed using Statview 5.0.1 (SAS Institute, Cary, NC) and GraphPad Prism 5.0 Software (San Diego, CA). Data were expressed as the mean ± standard error of the mean (SEM) of individual experiments. The number of independent experiments or the number of mice (n) used to ensure reproducibility is described in each figure legend. Repeated measures analysis of variance (ANOVA), two-way ANOVA, and two-tailed Student’s t-test were used for statistical analysis unless indicated otherwise in each figure legend. Changes were considered significant at p value < 0.05. Corrections for multiple comparisons were made as indicated in each experiment.

Extended Data

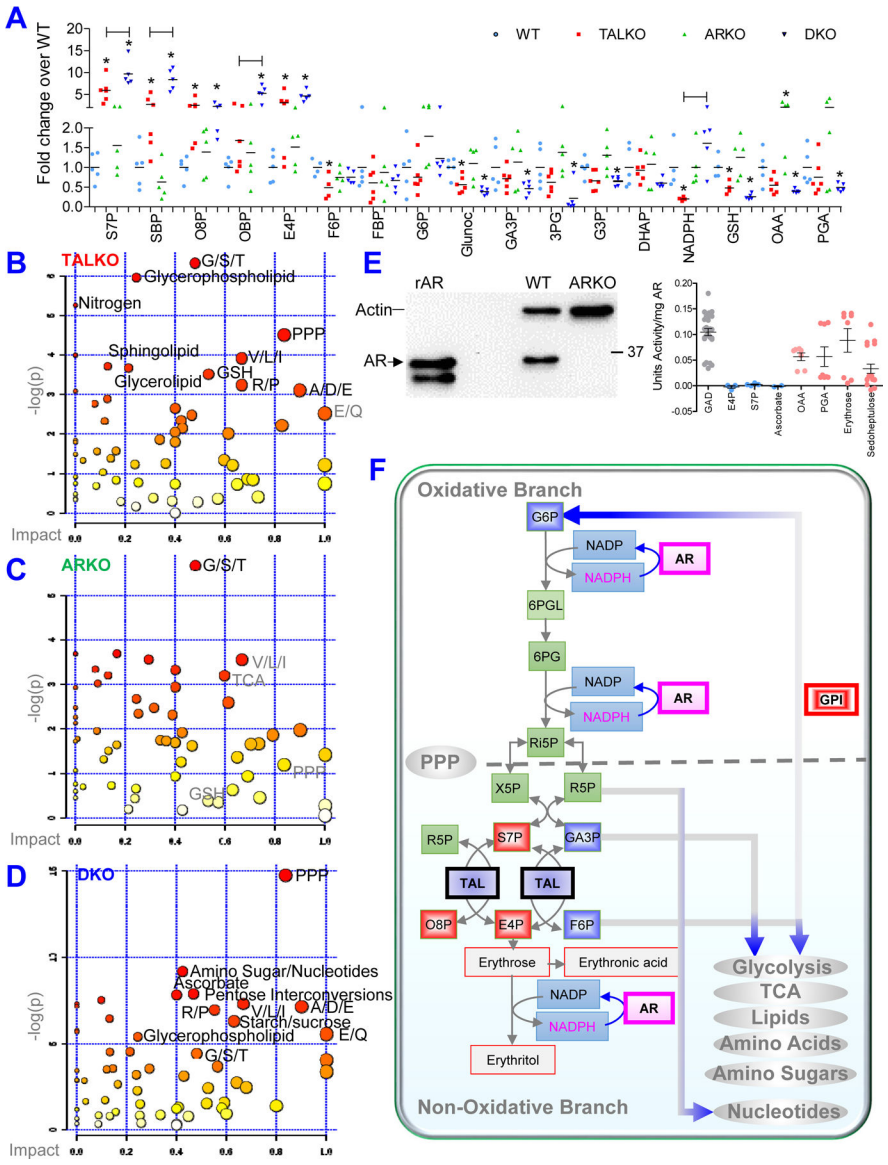

Extended Data Figure 1. Impact of AR on carbon recycling and NADPH output by PPP.

A, Bar chart shows opposite effects of AR inactivation on concentrations of substrates sequestered in the non-oxidative branch of the PPP with respect to those depleted in the oxidative PPP and connected pathways. Data represent individual and mean values from five mice per genotype. Changes in metabolite concentration affected by TAL deficiency at two-tailed t-test $p<0.05$ are shown. **B,** Global impact of TAL deficiency on the metabolome is indicated by analysis of pathways arranged according to the scores from enrichment analysis (y axis: −log p) and from topology analysis using betweenness centrality to estimate node importance (x axis: impact: number of detected metabolites with significant p value, using two-tailed t-test via Metaboanalyst). TAL deficiency most prominently impacted the PPP, glycerophospholipid, and glycine/serine/threonine (G/S/T), valine/leucine/isoleucine (V/L/I), and alanine, aspartate, glutamate (A/D/E) amino acid metabolism. **C,** Global impact

of AR deficiency on metabolic pathways, using two-tailed t-test via Metaboanalyst Pathway analysis module. **D,** Global impact of combined TAL and AR deficiency on metabolic pathways by comparison of DKO and WT mice, using two-tailed t-test via Metaboanalyst Pathway analysis module. **E,** Western blot detection recombinant AR (rAR, left panel) and assays of its enzyme activity (right panel). Data represent independent measurements for the following substrates: glyceraldehyde (GAD, n=28), ascorbate (n=2), E4P (n=3), S7P (n=4), OAA (n=7), PGA (n=8), erythrose (n=8), sedoheptulose (n=18). **F,** Schematic diagram of metabolic pathways affected by inactivation of the TAL-AR axis.

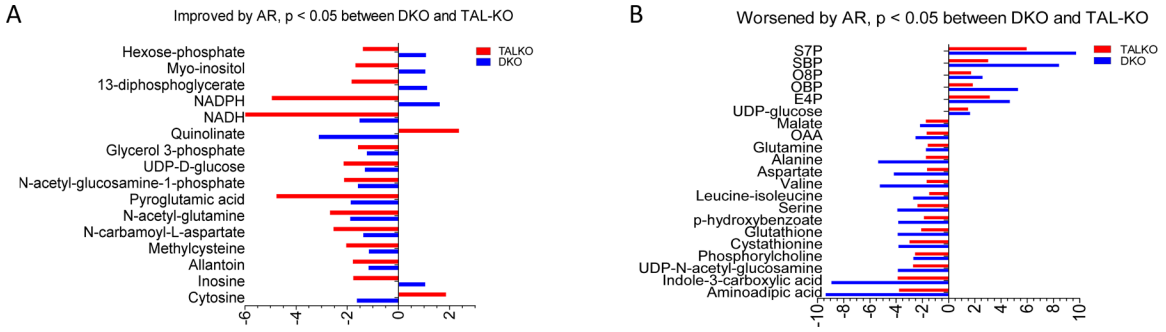

Extended Data Figure 2. Segregation of metabolites by impact of AR inactivation in TAL deficiency.

A, Metabolites affected synergistically by inactivation of the TAL-AR axis. **B,** Metabolite changes corrected by inactivation of AR. Displayed metabolites exhibited significant fold changes in TAL deficiency at two-tailed t-test $p < 0.05$.

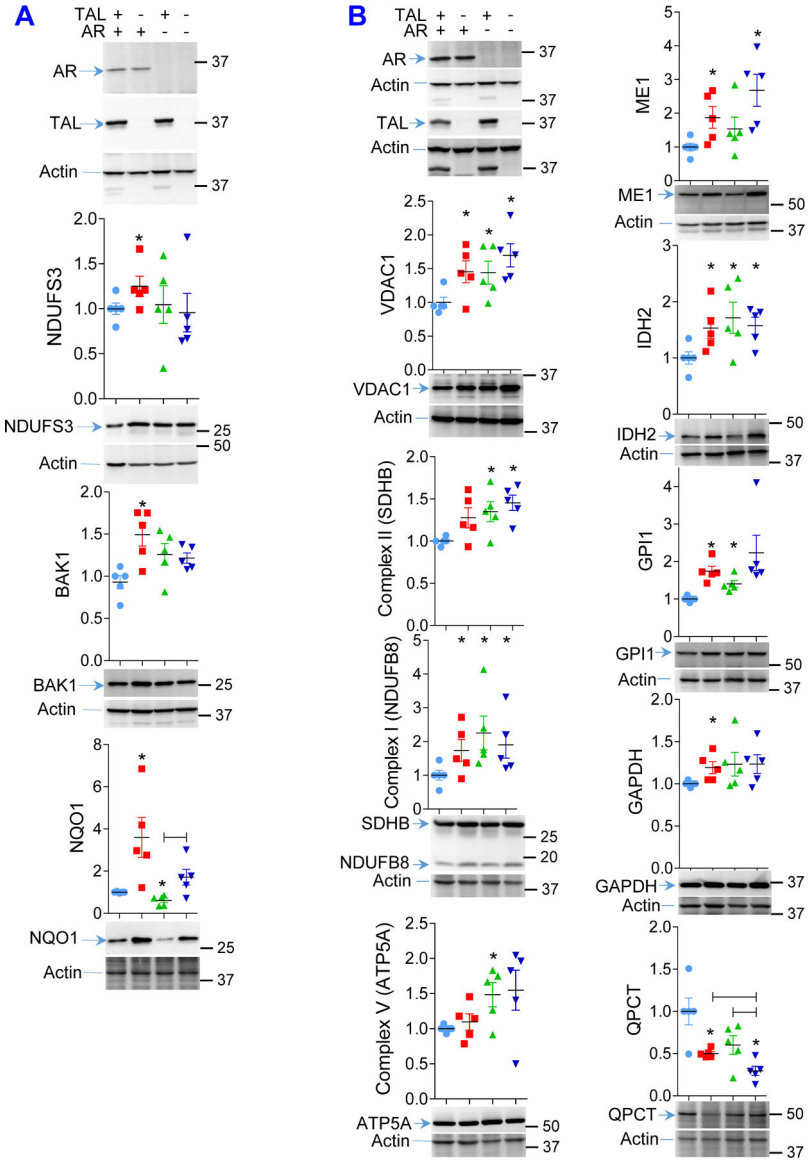

Extended Data Figure 3. Western blot analysis of expression in genes implicated by RNAseq changes in livers of TAL-deficient mice at FDR p< 0.05.

A, Western blot analysis of protein levels corrected by inactivation of AR. *, two-tailed t-test $p < 0.05$. **B**, Western blot analysis of protein levels uncorrected by inactivation of AR. Representative blots and bar charts of cumulative analysis of five mice per genotype are shown for each gene. *, two-tailed t-test $p < 0.05$.

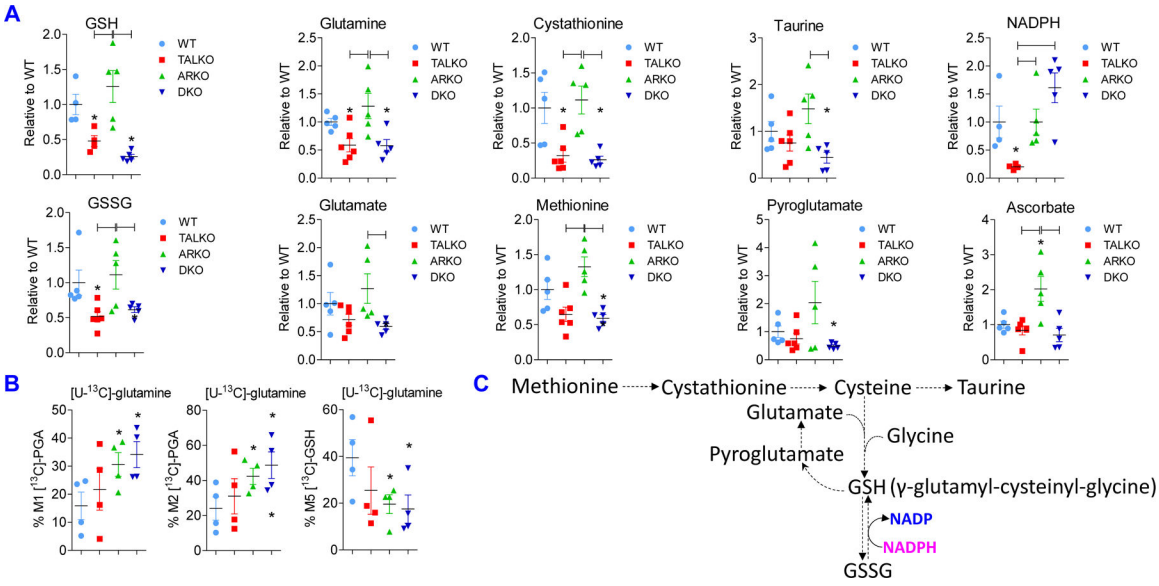

Extended Data Figure 4. Effect of the TAL-AR axis on *de novo* GSH biosynthesis.

A, Measurement of GSH synthesis intermediates in liver of WT (n=4), TALKO (n=4), ARKO (n=5), and DKO mice (n=5). *, $p < 0.05$ relative to WT using two-tailed t test. Brackets indicate differences between mouse strains at $p < 0.05$. **B,** Enrichment of [M1-^{13C}]-PGA, [M2-^{13C}]-PGA, and [M5-^{13C}]-GSH in hepatocytes of WT (n=4), TALKO (n=4), ARKO (n=4), and DKO mice (n=4) labelled with [U-^{13}C]-glutamine (DLM-1150–0.5, Cambridge Isotope Laboratories; Cambridge, MA) for 24 hours. *, $p < 0.05$ relative to WT using one-tailed t-test. **C,** Schematic diagram of GSH biosynthesis involving substrates regulated by the TAL-AR axis.

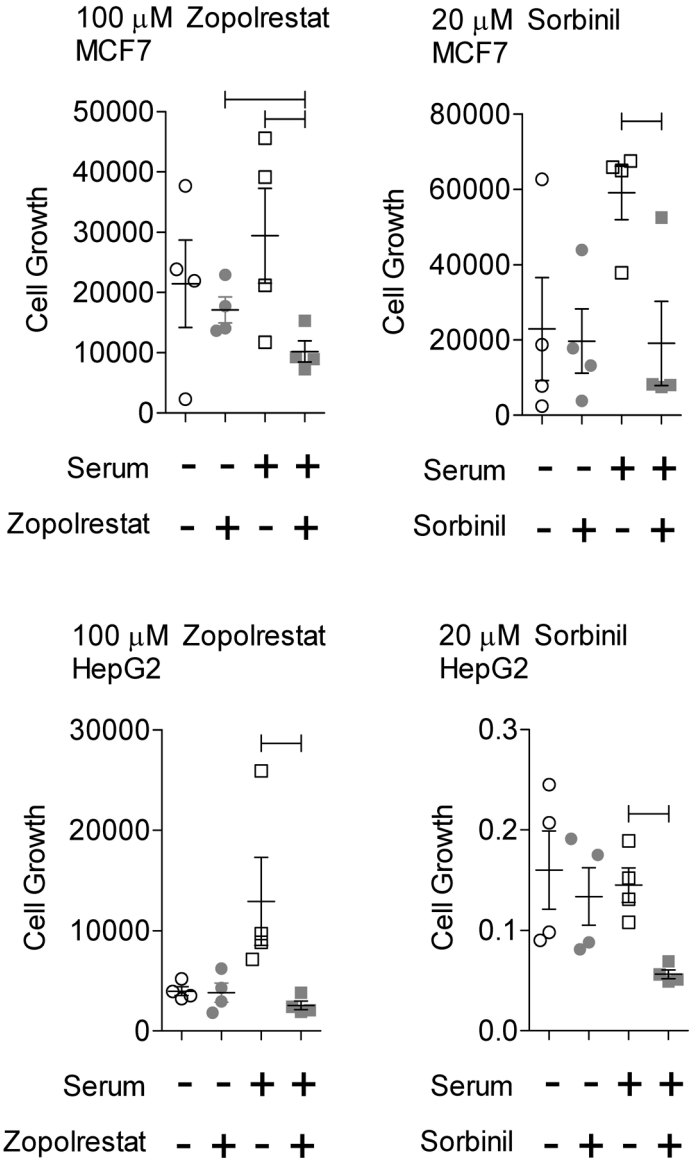

Extended Data Figure 5. Effect of aldose reductase inhibitors, zopolrestat and sorbinil, on serum replenishment-induced proliferation of HepG2 hepatoma and MCF7 breast carcinoma cells.

MCF7 or HepG2 cells seeded 96-well plates at 5,000 cells/well in complete Dulbecco's minimal essential medium with 10% fetal bovine serum (Hyclone, Logan, UT), 2 mM L-glutamine, 100 units/ml penicillin, 100 μg/ml streptomycin, 25 μg/ml amphotericin B (GIBCO/ThermoFisher catalogue number 15240096) at 37 °C with 5% CO2. After 24 hours, sub-confluent cells were growth arrested in 0.1% FBS with or without sorbinil (Millipore/Sigma catalogue number S7701) or zopolrestat (Millipore/Sigma catalogue number Z4527). After 24 h, 10% serum was added to the medium and the cells were incubated for another 24 h. Cells were counted after trypan blue staining (upper and lower left panels and upper right panel) and viability was evaluated by the 3-[4,5-dimethylthiazol-2-yl]-2,5 diphenyl tetrazolium bromide (MTT) assay (lower right panel) [1]. MTT powder was dissolved in PBS to a final concentration of 5 mg/ml, and 500 μl of MTT solution was added to cells and incubated for 1 h at 37°C. Subsequently, 500 μl of isopropyl

alcohol with 0.04 N HCl was added to dissolve the precipitate. Absorbance was read at the 570-nm wavelength subtracting background reading at the 650-nm wavelength. Data represent four experiments. Brackets reflect p values <0.05 as compared by 1-way ANOVA.

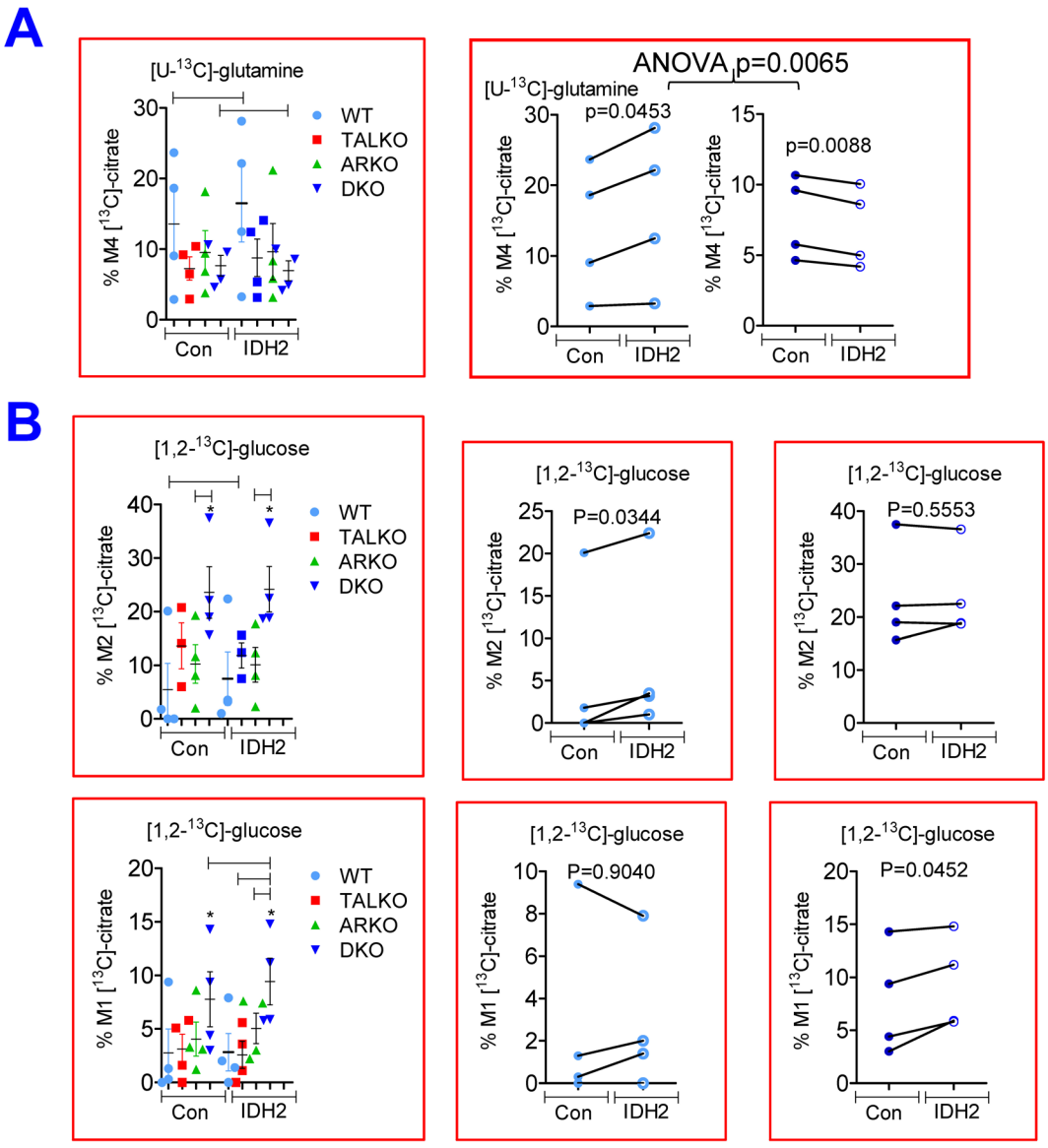

Extended Data Figure 6. Effect of siRNA-mediated knockdown of IDH2 on metabolic flux through the TCA cycle in primary hepatocytes from age-matched female WT, TALKO, ARKO, and DKO mice.

A, Effect of IDH2 knockdown on enrichment of [M4-^{13C}]-citrate in hepatocytes labelled with [U-^{13}C]-glutamine (DLM-1150–0.5, Cambridge Isotope Laboratories; Cambridge, MA) for 24 hours. **B,** Effect of IDH2 knockdown on enrichment of [M1-^{13C}]-citrate, and [M2-^{13C}]-citrate in hepatocytes labelled with [1, 2-^{13}C]-glucose (CLM-504–0.5, Cambridge Isotope Laboratories; Cambridge, MA) for 24 hours. Data represent mean ± SE of experiments using 4 WT, 4 TALKO, 4 ARKO, and 4 DKO mice. *, Brackets reflect p values 0.05 using unpaired two-tailed t tests for comparison of mice with different genotypes.

Effect of IDH2 knockdown was evaluated with two-tailed paired t-tests; p values <0.05 are displayed.

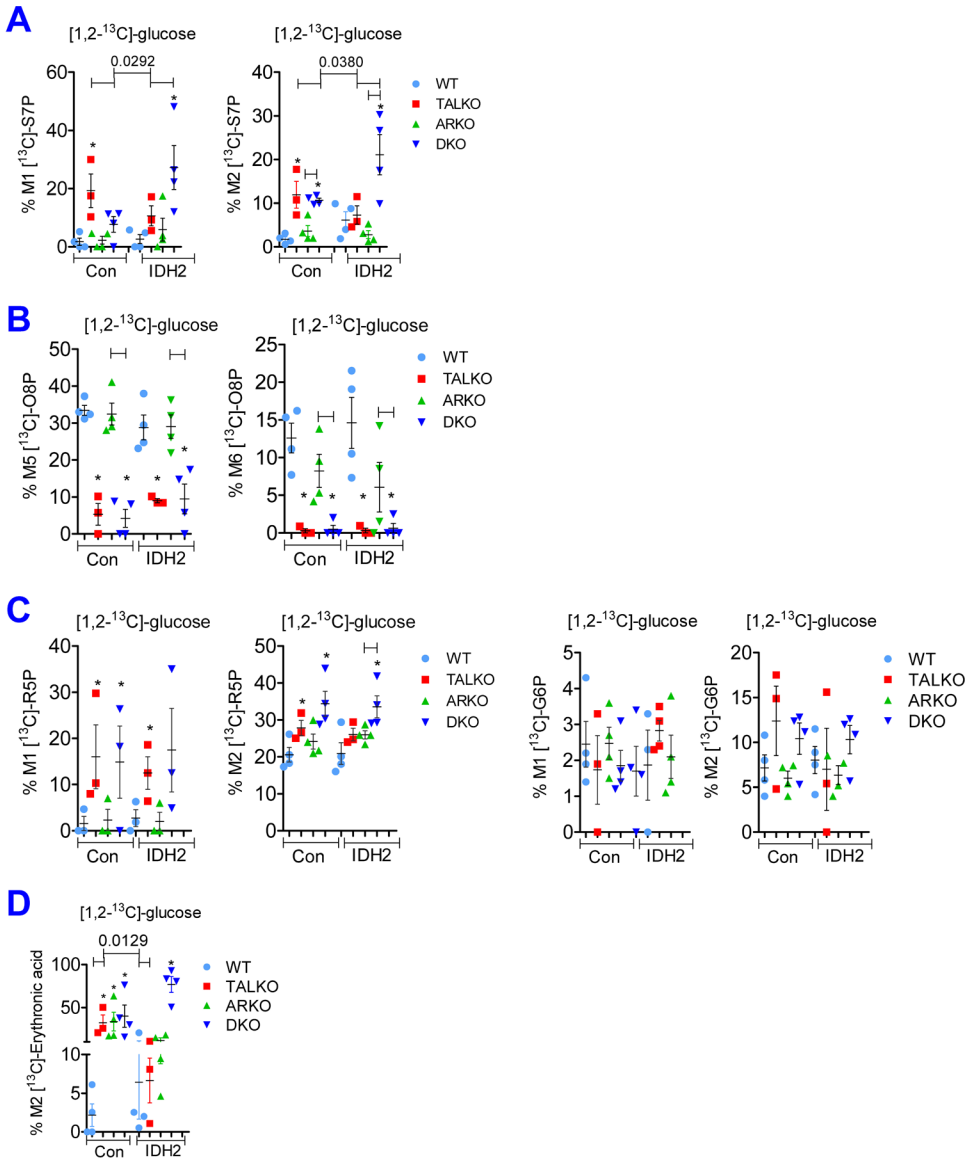

Extended Data Figure 7. IDH2 moderates carbon sequestration in the non-oxidative PPP in primary DKO hepatocytes.

A, Effect of IDH2 knockdown on enrichment of [M1-^{13C}]-S7P and [M2-^{13C}]-S7P in WT, TALKO, ARKO, and DKO hepatocytes labelled with [1, 2-^{13}C]-glucose (CLM-504–0.5, Cambridge Isotope Laboratories; Cambridge, MA) for 24 hours. **B,** Effect of IDH2 knockdown on enrichment of [M5-^{13C}]-O8P and [M6-^{13C}]-O8P in WT, TALKO, ARKO, and DKO hepatocytes labelled with [1, 2-^{13}C]-glucose (CLM-504–0.5, Cambridge Isotope Laboratories; Cambridge, MA) for 24 hours. **C,** Effect of IDH2 knockdown on enrichment of [M1-^{13C}]-R5P and [M2-^{13C}]-R5P and [M1-^{13}C]-G6P and [M2-^{13}C]-G6P in WT, TALKO, ARKO, and DKO hepatocytes labelled with [1, 2-^{13}C]-glucose (CLM-504–0.5, Cambridge Isotope Laboratories; Cambridge, MA) for 24 hours. **D,** Effect of IDH2

knockdown on enrichment of [M2-^{13C}]-erythronic acid in WT, TALKO, ARKO, and DKO hepatocytes labelled with [1, 2-^{13}C]-glucose (CLM-504–0.5, Cambridge Isotope Laboratories; Cambridge, MA) for 24 hours. Data represent mean ± SE of experiments using 4 WT, 3 TALKO, 4 ARKO, and 4 DKO mice. *, $p < 0.05$ relative to WT using unpaired two-tailed t tests. Brackets reflect p values 0.05 using 2-way ANOVA.

Supplementary Material

Refer to Web version on PubMed Central for supplementary material.

Acknowledgements

This work was supported in part by grants RO1 DK078922 (APe), R01 AI072648 (APe), P30CA006516 (J.M.A.) and P01CA120964 (J.M.A.) from the National Institutes of Health, and the Central New York Community Foundation (APe).

Data availability.

All original data will be available through sharing and Databases with accession codes provided by the time of publication. RNA-sequencing data have been deposited in the NCBI Gene Expression Omnibus database (Accession GSE217133).

REFERENCES

1. Sung H et al. Global Cancer Statistics 2020: GLOBOCAN Estimates of Incidence and Mortality Worldwide for 36 Cancers in 185 Countries. CA Cancer J. Clin 71, 209–249 (2021). [PubMed: 33538338]
2. Perl A, Hanczko R, Telarico T, Oaks Z, & Landas S Oxidative stress, inflammation and carcinogenesis are controlled through the pentose phosphate pathway by transaldolase. Trends Mol. Med 7, 395–403 (2011).
3. Nelson ME et al. Inhibition of hepatic lipogenesis enhances liver tumorigenesis by increasing antioxidant defence and promoting cell survival. Nat. Commun. 8, (2017).
4. Choi JE et al. A unique subset of glycolytic tumour-propagating cells drives squamous cell carcinoma. Nat. Metab 3, 182–195 (2021). [PubMed: 33619381]
5. Sullivan L et al. The Proto-oncometabolite Fumarate Binds Glutathione to Amplify ROS-dependent signaling. Mol. Cell 51, 236–248 (2013). [PubMed: 23747014]
6. Horecker BL The pentose phosphate pathway. J. Biol. Chem 277, 47965–47971 (2002). [PubMed: 12403765]
7. Li M et al. Aldolase B suppresses hepatocellular carcinogenesis by inhibiting G6PD and pentose phosphate pathways. Nat. Cancer 1, 735–747 (2020). [PubMed: 35122041]
8. Vulliamy T, Mason P, & Luzzatto L The molecular basis of glucose-6-phosphate dehydrogenase deficiency. [Review] [41 refs]. Trends Genet 8, 138–143 (1992). [PubMed: 1631957]
9. Pandolfi PP, Sonati F, Rivi R, Mason P, & Grosveld F Targeted disruption of the housekeeping gene encoding glucose 6- phosphate dehydrogenase (G6PD): G6PD is dispensable for pentose synthesis but essential for defense against oxidative stress. EMBO J 14, 5209–5215 (1995). [PubMed: 7489710]
10. Perl A et al. Transaldolase is essential for maintenance of the mitochondrial transmembrane potential and fertility of spermatozoa. Proc. Natl. Acad. Sci. USA 103, 14813–14818 (2006). [PubMed: 17003133]
11. Hanczko R et al. Prevention of hepatocarcinogenesis and acetaminophen-induced liver failure in transaldolase-deficient mice by N-acetylcysteine. J. Clin. Invest 119, 1546–1557 (2009). [PubMed: 19436114]

12. LeDuc C et al. Novel Association of Early Onset Hepatocellular Carcinoma with Transaldolase Deficiency. JIMD Rep 12, 121–127 (2014). [PubMed: 24097415]
13. Grammatikopoulos T et al. Liver Disease and Risk of Hepatocellular Carcinoma in Children With Mutations in TALDO1. Hepatol. Commun n/a, (2021).
14. Williams M et al. Clinical, biochemical, and molecular overview of transaldolase deficiency and evaluation of the endocrine function: Update of 34 patients. J. Inher. Metab. Dis 42, 147–158 (2019). [PubMed: 30740741]
15. Qian Y et al. Transaldolase deficiency influences the pentose phosphate pathway, mitochondrial homoeostasis and apoptosis signal processing. Biochem. J 415, 123–134 (2008). [PubMed: 18498245]
16. Oaks Z et al. Transaldolase haploinsufficiency in subjects with acetaminophen-induced liver failure. J. Inherit. Metab. Dis 43, 496–506 (2020). [PubMed: 31769880]
17. Jones BE, Liu H, Lo CR, Koop DR, & Czaja MJ Cytochrome P450 2E1 Expression Induces Hepatocyte Resistance to Cell Death from Oxidative Stress. Antiox. Redox Signal 4, 701–709 (2002).
18. Dahlin DC, Miwa GT, Lu AY, & Nelson SD N-acetyl-p-benzoquinone imine: a cytochrome P-450-mediated oxidation product of acetaminophen. !Lost Data 81, 1327–1331 (1984).
19. Vas,Gy. et al. Study of transaldolase deficiency in urine samples by capillary LC-MS/MS. J. Mass. Spec 41, 463–469 (2005).
20. Wilmarth PA et al. A systems approach implicates nuclear receptor targeting in the Atp7b −/− mouse model of Wilson's disease. Metallomics 4, 660–668 (2012). [PubMed: 22565294]
21. Nordgaard C et al. ZAK-b activated by cellular compression and mediates contraction-induced MAP kinase signaling in skeletal muscle. EMBO J n/a, e111650 (2022). [PubMed: 35899396]
22. Lee KW, Ko BC, Jiang Z, Cao D, & Chung SS Overexpression of aldose reductase in liver cancers may contribute to drug resistance. Anticancer Drugs 12, 129–132 (2001). [PubMed: 11261885]
23. Rodan LH & Berry GT N-Acetylcysteine Therapy in an Infant with Transaldolase Deficiency Is Well Tolerated and Associated with Normalization of Alpha Fetoprotein Levels. JIMD Rep 31, 73–77 (2016). [PubMed: 27130472]
24. El-Serag HB Hepatocellular carcinoma: Recent trends in the United States. Gastroenterology 127, S27–S34 . [PubMed: 15508094]
25. Koutselini H, Lazaris AC, Kavantzas N, Kiritsi T, & Davaris PS Significance of nuclear morphometry as a diagnostic tool in fine-needle aspirates of the liver. Eur. J. Gastroenterol. Hepatol 12, 913–921 (2000). [PubMed: 10958219]
26. Lee-Barber J et al. Apparent Acetaminophen Toxicity in a Patient with Transaldolase Deficiency. JIMD Rep 44, 9–15 (2019). [PubMed: 29923087]
27. Lee WM Acetaminophen and the U.S. Acute Liver Failure Study Group: lowering the risks of hepatic failure.[see comment]. [Review] [22 refs]. Hepatology 40, 6–9 (2004). [PubMed: 15239078]
28. Jang C, Chen L, & Rabinowitz JD Metabolomics and Isotope Tracing. Cell 173, 822–837 (2018). [PubMed: 29727671]
29. Oaks Z et al. Mitochondrial dysfunction in the liver and antiphospholipid antibody production precede disease onset and respond to rapamycin in lupus-prone mice. Arthritis Rheumatol 68, 2728–2739 (2016). [PubMed: 27332042]
30. Kim TW et al. NQO1 Deficiency Leads Enhanced Autophagy in Cisplatin-Induced Acute Kidney Injury Through the AMPK/TSC2/mTOR Signaling Pathway. Antioxid. Redox Signal 24, 867–883 (2016). [PubMed: 26935540]
31. Koch B et al. Crystal Structures of Glutaminyl Cyclases (QCs) from Drosophila melanogaster Reveal Active Site Conservation between Insect and Mammalian QCs. Biochemistry 51, 7383–7392 (2012). [PubMed: 22897232]
32. Wellner VP, Sekura R, Meister A, & Larsson A Glutathione Synthetase Deficiency, an Inborn Error of Metabolism Involving the g-Glutamyl Cycle in Patients with 5-Oxoprolinuria (Pyroglutamic Aciduria). !Lost Data 71, 2505–2509 (1974).

33. Zhong H et al. Mitochondrial control of apoptosis through modulation of cardiolipin oxidation in hepatocellular carcinoma: A novel link between oxidative stress and cancer. Free Rad. Biol. Med 102, 67–76 (2017). [PubMed: 27838437]
34. Shi F et al. Oxidative damage of DNA, RNA and their metabolites in leukocytes, plasma and urine of Macaca mulatta: 8-oxoguanosine in urine is a useful marker for aging. Free Rad. Res 46, 1093–1098 (2012).
35. Soga T et al. Differential Metabolomics Reveals Ophthalmic Acid as an Oxidative Stress Biomarker Indicating Hepatic Glutathione Consumption. J. Biol. Chem 281, 16768–16776 (2006). [PubMed: 16608839]
36. Gao N et al. Hyperhomocysteinemia-Induced Oxidative Stress Aggravates Renal Damage in Hypertensive Rats. Am. J. Hypertens 33, 1127–1135 (2020). [PubMed: 32484231]
37. Hayashi M et al. High Serum Uric Acid Levels Could Be a Risk Factor of Hepatocellular Carcinoma Recurrences. Nutr. Cancer 73, 996–1003 (2021). [PubMed: 32538144]
38. Murphy MP How mitochondria produce reactive oxygen species. Biochem. J 417, 1–13 (2009). [PubMed: 19061483]
39. Kadenbach B Intrinsic and extrinsic uncoupling of oxidative phosphorylation. Biochim. Biophys. Acta 1604, 77–94 (2003). [PubMed: 12765765]
40. De la Fuente IM et al. On the dynamics of the adenylate energy system: homeorhesis vs homeostasis. PLoS ONE 9, e108676 (2014). [PubMed: 25303477]
41. Vander Heiden MG, Cantley LC, & Thompson CB Understanding the Warburg Effect: The Metabolic Requirements of Cell Proliferation. Science 324, 1029–1033 (2009). [PubMed: 19460998]
42. Zhang J et al. 13C isotope-assisted methods for quantifying glutamine metabolism in cancer cells. Meth. Enzymol 542, 369–389 (2014).
43. Engelke UFH et al. Mitochondrial involvement and erythronic acid as a novel biomarker in transaldolase deficiency. Biochim. Biophys. Acta 1802, 1028–1035 (2010). [PubMed: 20600873]
44. Kotas ME & Medzhitov R Homeostasis, Inflammation, and Disease Susceptibility. Cell 160, 816–827 (2015). [PubMed: 25723161]
45. Sohn MJ AUID et al. Metabolomic Signatures for the Effects of Weight Loss Interventions on Severe Obesity in Children and Adolescents LID - 10.3390/metabo12010027 [doi] LID - 27.
46. Giustarini D et al. Assessment of glutathione/glutathione disulphide ratio and S-glutathionylated proteins in human blood, solid tissues, and cultured cells. Free Radic. Biol. Med 112, 360–375 (2017). [PubMed: 28807817]
47. Mueller CFH et al. The Role of the Multidrug Resistance Protein-1 in Modulation of Endothelial Cell Oxidative Stress. Circ. Res 97, 637 (2005). [PubMed: 16123331]
48. Ishikawa T & Sies H Cardiac transport of glutathione disulfide and S-conjugate. Studies with isolated perfused rat heart during hydroperoxide metabolism. J. Biol. Chem 259, 3838–3843 (1984). [PubMed: 6706982]
49. Oates PJ Aldose reductase, still a compelling target for diabetic neuropathy. Curr. Drug Targ 9, 14–36 (2008).
50. Thakur S, Gupta SK, Ali V, Singh P, & Verma M Aldose Reductase: a cause and a potential target for the treatment of diabetic complications. Arch. Pharm. Res 44, 655–667 (2021). [PubMed: 34279787]
51. Lovat PE et al. Bak: A Downstream Mediator of Fenretinide-Induced Apoptosis of SH-SY5Y Neuroblastoma Cells. Cancer Res 63, 7310–7313 (2003). [PubMed: 14612528]
52. Tarrio N, Garcia-Leiro A, Cerdan ME, & Gonzalez-Siso MI The role of glutathione reductase in the interplay between oxidative stress response and turnover of cytosolic NADPH in Kluyveromyces lactis. FEMS Yeast Research 8, 597–606 (2008). [PubMed: 18318708]
53. Racker E & Schroeder E Formation and utilization of octulose-8-phosphate by transaldolase and transketolase. Arch. Biochem. Biophys 66, 241–243 (1957).
54. Paoletti F, Williams JF, & Horecker BL Detection and estimation of sedoheptulose and octulose mono- and bisphosphates in extracts of rat liver. Arch. Biochem. Biophys 198, 620–626 (1979). [PubMed: 518101]

55. Stincone A et al. The return of metabolism: biochemistry and physiology of the pentose phosphate pathway. Biol. Rev 90, 927–963 (2015). [PubMed: 25243985]
56. Kovarova J et al. Deletion of transketolase triggers a stringent metabolic response in promastigotes and loss of virulence in amastigotes of Leishmania mexicana. PLoS Pathog 14, e1006953 (2018). [PubMed: 29554142]
57. Fukumoto S.i. et al. Overexpression of the Aldo-Keto Reductase Family Protein AKR1B10 Is Highly Correlated with Smokers' Non-Small Cell Lung Carcinomas. Clin Cancer Res 11, 1776 (2005). [PubMed: 15755999]
58. Ma J et al. AKR1B10 overexpression in breast cancer: Association with tumor size, lymph node metastasis and patient survival and its potential as a novel serum marker. Int. J. Cancer 131, E862–E871 (2012). [PubMed: 22539036]
59. Ho HT et al. Aldose reductase-deficient mice develop nephrogenic diabetes insipidus. Mol. Cell. Biol 20, 5840–5846 (2000). [PubMed: 10913167]
60. Edmondson HA & Steiner PE Primary carcinoma of the liver. A study of 100 cases among 48,900 necropsies. Cancer 7, 462–503 (1954). [PubMed: 13160935]
61. International Consensus Group for Hepatocellular Neoplasia Pathologic diagnosis of early hepatocellular carcinoma: A report of the international consensus group for hepatocellular neoplasia. Hepatology 49, 658–664 (2009). [PubMed: 19177576]
62. Yuan M, Breitkopf SB, Yang X, & Asara JM A positive/negative ion-switching, targeted mass spectrometry-based metabolomics platform for bodily fluids, cells, and fresh and fixed tissue. Nat. Prot 7, 872–881 (2012).
63. Xia J, Broadhurst DI, Wilson M, & Wishart DS Translational biomarker discovery in clinical metabolomics: An introductory tutorial. Metabolomics 9, 280–299 (2013). [PubMed: 23543913]
64. Barski OA, Gabbay KH, Grimshaw CE, & Bohren KM Mechanism of human aldehyde reductase: characterization of the active site pocket. Biochemistry 34, 11261–11275 (1995).
65. Banki K, Halladay D, & Perl A Cloning and expression of the human gene for transaldolase: a novel highly repetitive element constitutes an integral part of the coding sequence. J. Biol. Chem 269, 2847–2851 (1994). [PubMed: 8300619]

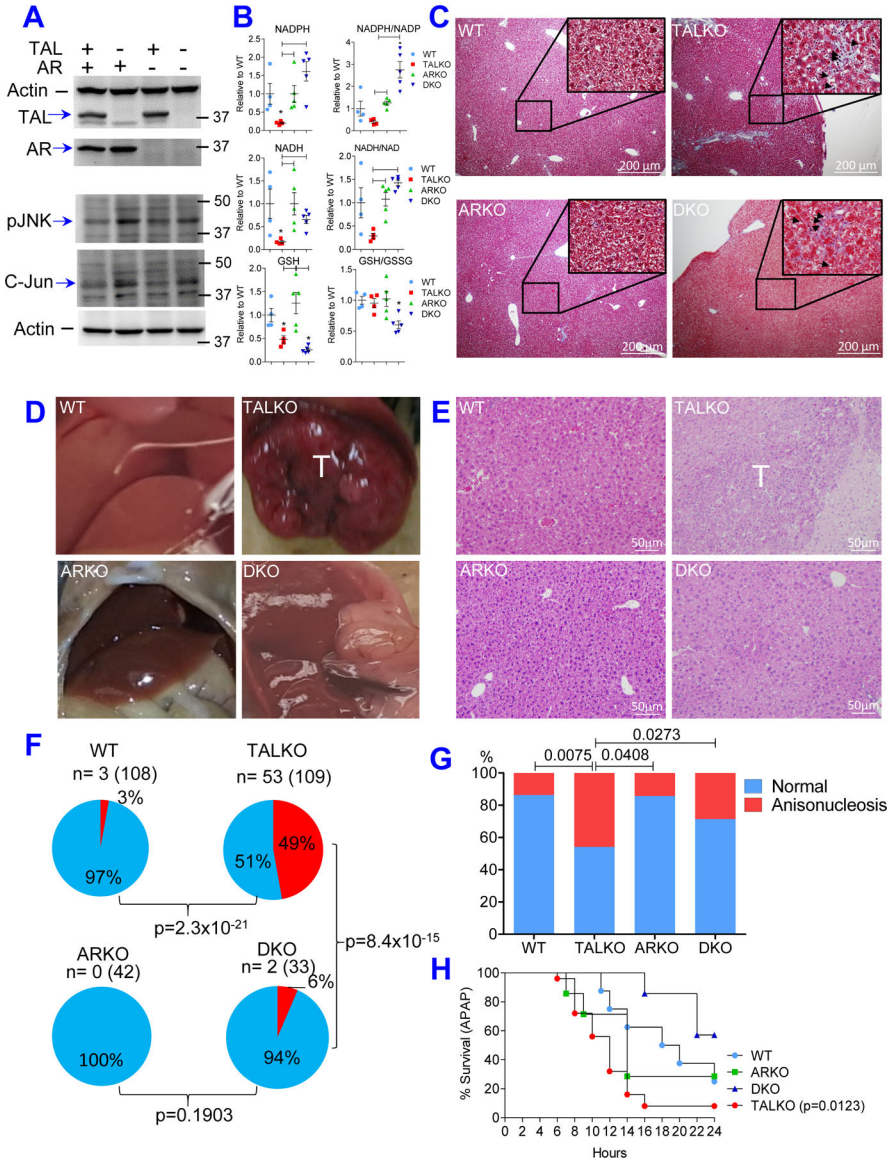

Figure 1. Inactivation of AR blocks hepatocarcinogenesis and susceptibility to APAP in TAL deficiency.

A, Western blot analyses of TAL, AR, pJNK, and c-jun in livers from wild-type (WT or $TAL^{+/+}AR^{+/+}$), TAL-deficient (TALKO or $TAL^{-/-}AR^{+/+}$), AR-deficient (ARKO or $TAL^{+/+}AR^{-/-}$), and double-deficient (DKO, or $TAL^{-/-}AR^{-/-}$) mice. **B**, Measurement of NADPH and GSH by LC-MS/MS. Data represent mean ± SEM of measurements were carried out from liver extracts of 4 mice per each genotype. Using two-tailed t-test, differences at $p < 0.05$ relative to WT are indicated by *; differences at $p < 0.05$ between other mouse strains are indicated by brackets. **C**, Detection of fibrosis in Gömöri-trichrome-stained liver tissues from TALKO and DKO mice. Pro-fibrotic Ito cells or fat-storing hepatic stellate cells are indicated with arrows in areas of higher magnification. Stellate cells were expanded in livers of TALKO (4.75-fold; p=0.007) and DKO mice relative to WT controls (6-fold; p=0.042). **D**, Detection of tumor (T) in TALKO but not in WT, ARKO, and DKO livers. **E**, Microscopy of tumor (T) reveals hepatocellular carcinoma (HCC) in TALKO liver.

F, Frequency of HCC in WT, TALKO, ARKO, and DKO mice aged to 78 weeks. The number of animals that developed HCC is indicated: n; the total number of animals per genotype is shown in parenthesis; p values reflect comparison with two-tailed Fisher's exact test. **G**, Prevalence of anisonucleosis was increased in TALKO mice relative to WT controls; p value reflect comparison with two-tailed chi-square test. **H**, Survival of WT, TALKO, ARKO, and DKO mice following APAP exposure. Percent survival of seven or more mice per strain were compared to eight WT mice by Mantel-Cox log-rank test using GraphPad software.

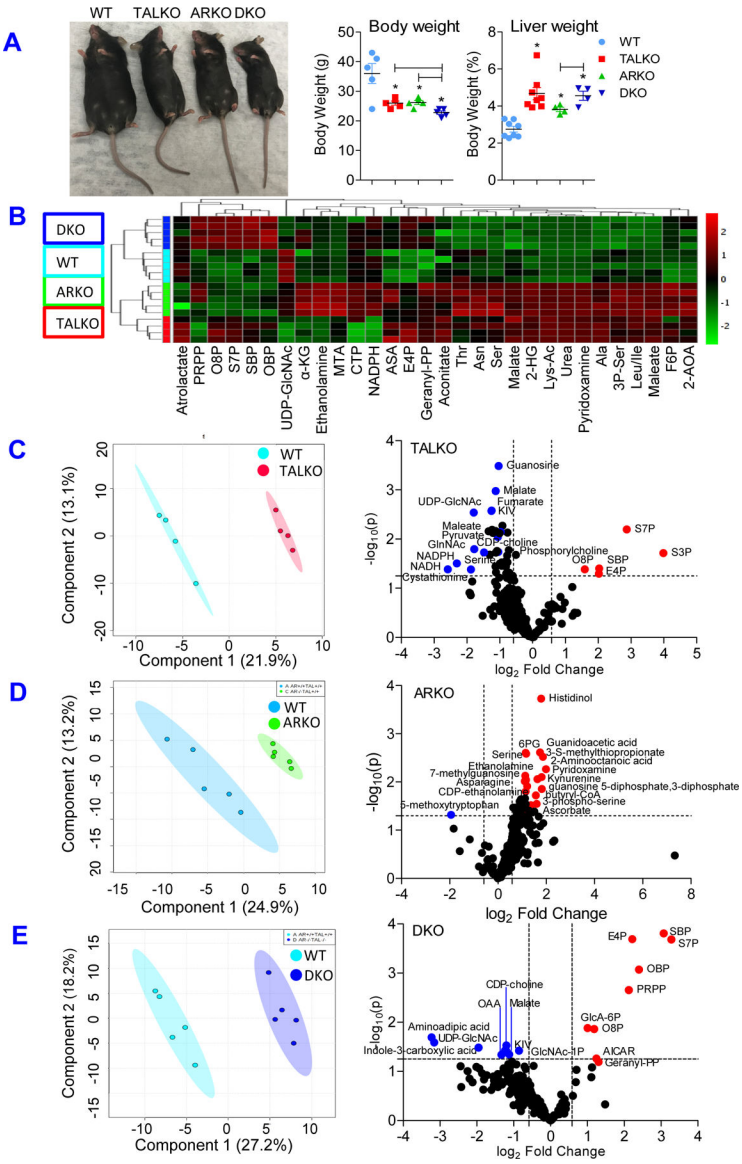

Figure 2. TAL-AR axis controls growth and body size through carbon trapping in the non-oxidative branch of the PPP.

A, Representative images of body size (left panel) and cumulative weight differences at 24 weeks of age among WT, TALKO, ARKO, and DKO female mice (right panel). Data represent mean ± SE of five mice per genotype. Using two-tailed t-test, differences at $p < 0.05$ relative to WT are indicated by *; differences at $p < 0.05$ between other mouse strains are indicated by brackets. **B**, Metabolome analysis by LC-MS/MS shows progressive trapping of 4–8 carbon sugars in the non-oxidative branch of the PPP by inactivation of the TAL-AR axis. Heat diagrams show genotype-dependent changes of the top 30 metabolites. The color bar on the right side of the heat diagram depicts two-fold changes into positive (red) or negative direction (green) relative to the mean of each compound. **C**, Discrimination of the metabolomes of TALKO and WT mice by PLS-DA (left panel) and volcano plot (right panel). **D**, Discrimination of the metabolomes of ARKO and WT mice by PLS-DA (left panel) and volcano plot (right panel). **E**, Discrimination of the liver metabolomes of

DKO and WT mice by PLS-DA (left panel) and volcano plot (right panel). The log2FC fold change and -log10p cut-off values in volcano plots of panels C-E were 2-fold and $p<0.05$, respectively.

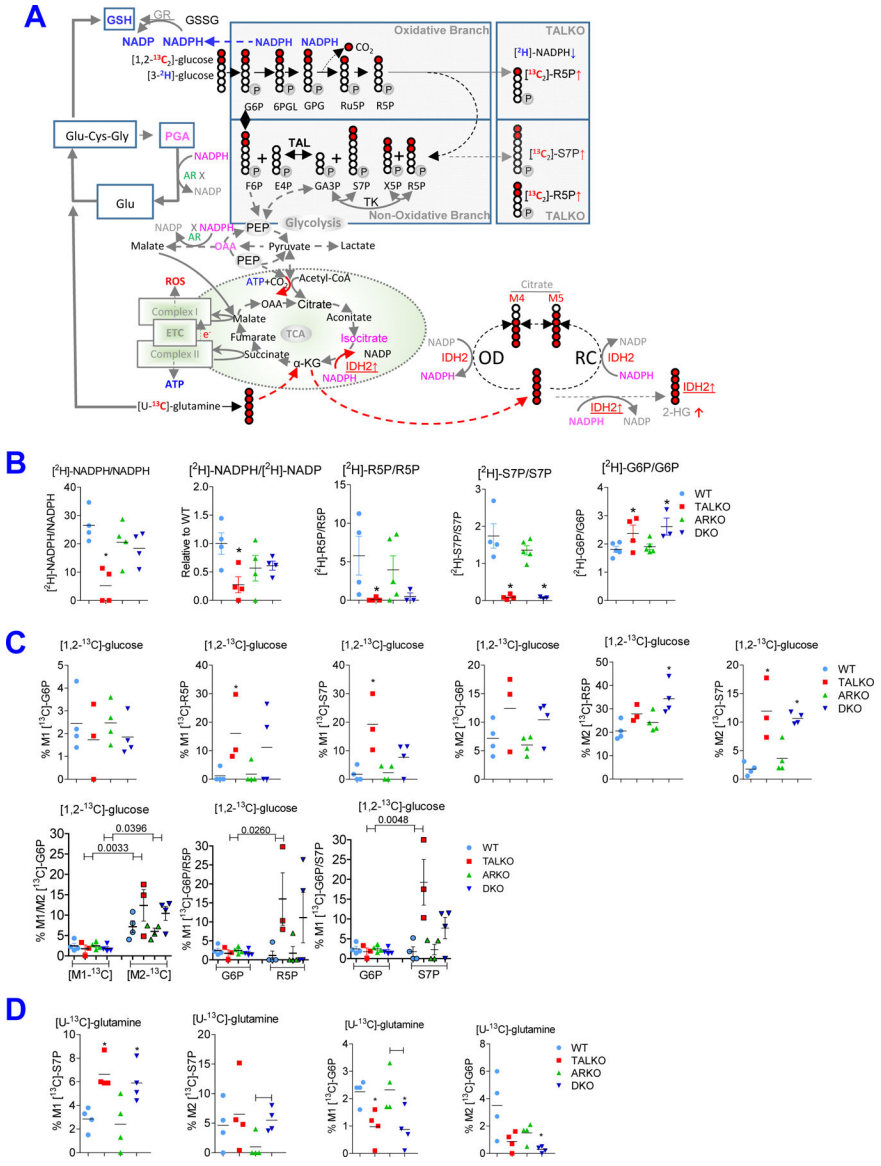

Figure 3. Effect of TAL, AR, and dual TAL and AR deletion on NADPH production and metabolic flux through the PPP in primary hepatocytes.

A, Schematic diagram of stable isotope labeling and tracing of isotopologue distributions across the PPP, glycolysis, and the TCA cycle. Hepatocytes were labelled with [3-^{2}H]-glucose to assess NADPH production by the PPP, [1,2-^{13}C]-glucose to assess carbon flux via the PPP, and [U-^{13}C]-glutamine to assess carbon flux through the TCA cycle. Red circles mark ^{13}C label within glucose or glutamine. Metabolites in blue are depleted in TALKO hepatocytes. NADPH molecules in purple are connected to enzyme reactions of regulatory impact, which are catalyzed by AR and IDH2. **B**, Enrichment of [3-^{2}H]-NADPH in hepatocytes labelled with [3-^{2}H]-glucose (DLM-9294-PK, Cambridge Isotope Laboratories; Cambridge, MA) for 24 hours. Hydride formation was also noted in NADP, R5P, S7P, and G6P. **C**, Enrichment of [M1-^{13}C]-S7P and [M2-^{13}C]-S7P in hepatocytes labelled with [1, 2-^{13}C]-glucose (CLM-504–0.5, Cambridge Isotope Laboratories; Cambridge, MA) for 24 hours. **D**, Enrichment of [M1-^{13}C]-S7P and [M2-^{13}C]-S7P and [M1-^{13}C]-G6P and

[M2-^{13}C]-G6P in hepatocytes labelled with [U-^{13}C]-glutamine (DLM-1150–0.5, Cambridge Isotope Laboratories; Cambridge, MA) for 24 hours. Percent enrichment of labelled metabolites was calculated between cells cultured with and without stable isotopes. Data represent mean ± SE of experiments using 4 WT, 4 TALKO, 5 ARKO, and 5 DKO mice. *, $p<0.05$ reflect comparison with unpaired two-tailed t tests.

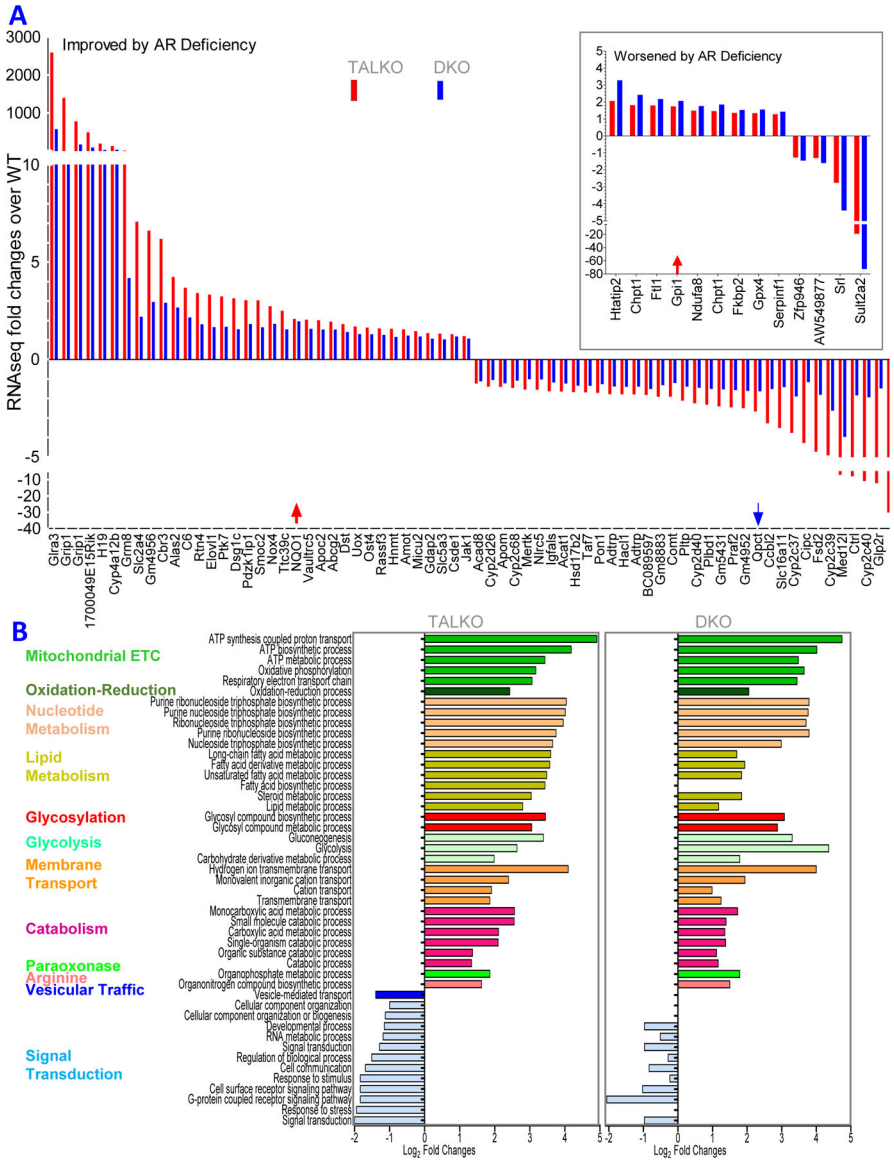

Figure 4. Impact of AR inactivation on changes in gene transcription imposed by TAL deficiency.

The signaling cascade triggered by TAL deficiency and modulated by AR inactivation was evaluated by sequencing of RNA from livers of disease-free, 14–16-week-old, age-matched female WT, TALKO, ARKO, and DKO mice, 5 mice from each genotype. Out of 24,606 RNA sequences identified, 300 were significantly affected by TAL deficiency at a false discovery rate (FDR) p value < 0.05 (Supplementary Table 1). **A**, Segregation of changes in gene expression by impact of AR inactivation in TAL deficiency. Abnormal expression of 70 genes was improved, while expression of 13 genes was further distorted by inactivation of AR. Blue and red arrows indicate decreases and increases of gene expression, which have been confirmed on the protein level by western blot analyses. **B**, Impact of gene expression changes on biological processes after Bonferroni correction for multiple comparisons. Statistical analysis was performed using Panther gene ontology software (http://www.pantherdb.org/pathway). Pathway changes represent the input 300 genes in TAL

mice and 526 genes in DKO mice, which were changed at FDR $p<0.05$ relative to WT controls.

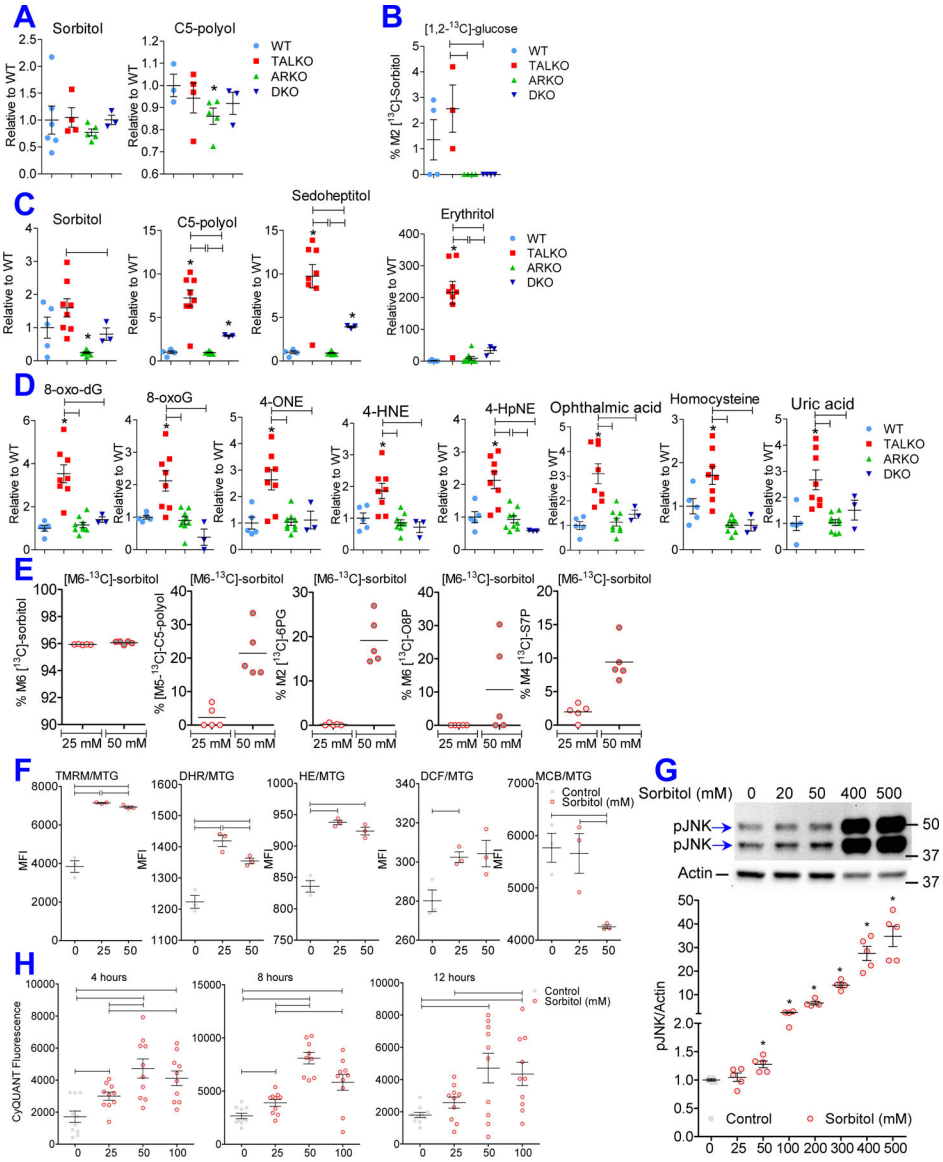

Figure 5. AR inactivation moderates the formation of polyols.

A, Steady state levels of C5-polyols and sorbitol in liver of WT (n=7), TALKO (n=6), ARKO (n=7), and DKO mice (n=8). Data represent mean ± SEM. Statistical analyses for all figure panels were performed with two-tailed t-test.*, $p < 0.05$ relative to WT. **B,** Enrichment of [M2-^{13}C]-sorbitol in hepatocytes labelled with [1, 2-^{13}C]-glucose (CLM-504–0.5, Cambridge Isotope Laboratories; Cambridge, MA) for 24 hours. Data represent mean ± SE of experiments using 4 WT, 4 TALKO, 5 ARKO, and 5 DKO mice. Statistical analyses for all figure panels were performed with two-tailed t-test. Brackets indicate differences between mouse strains at $p < 0.05$. **C**, Accumulation of sorbitol, C5-polyols, sedoheptitol, and erythritol in the urine of age-matched WT, TALKO, ARKO, and DKO mice. Metabolite concentrations were measured by LC-MS/MS and normalized to the mean of WT mice set at 1.0. Data represent mean ± SE of experiments using 5 WT, 8 TALKO, 9 ARKO, and 3 DKO mice. Statistical analyses for all figure panels were

performed with two-tailed t-test. Brackets indicate differences between mouse strains at $p < 0.05$. **D**, Biomarkers of increased oxidative stress in the urine of age-matched WT (n=7), TALKO (n=6), ARKO (n=7), and DKO mice (n=8). Lipid hydroperoxides 4-hydroperoxy-2-nonenal (4-HpNE), 4-oxo-2-nonenal (4-ONE), and 4-hydroxy-2-nonenal (4-HNE), oxidized DNA 8-oxoguanine (8-oxoG) and 8-oxo-2-deoxyguanosine (8-oxo-dGuo), ophthalmic acid, and homocysteine were measured by LC-MS/MS. Data represent mean ± SEM of concentration values normalized to the mean WT mice set at 1.0. Statistical analyses for all figure panels were performed with two-tailed t-test. Brackets indicate differences between mouse strains at $p < 0.05$. **E**, Metabolism of sorbitol by 1875 TALKO hepatoma cells. 75,000 cells were cultured for 24 hours in 6-well plates and labelled with 25 mM or 50 mM [M6-^{13}C]-sorbitol for 30 min (Cat. No. CLM-8529-PK, Cambridge Isotope Laboratories Inc., Tewksbury, MA). Before harvesting, 0.0125 mM 5-thio-glucose, an internal standard, was added to each well. Metabolite concentrations were measured by LC-MS/MS and normalized to the internal standard. Values are expressed as fold changes relative to the mean of control cells set at 1.0. Data represent mean ± SEM of 5 experiments. **F**, Effect of sorbitol on mitochondrial ROS production by 1875 TALKO hepatoma cells. 75,000 cells were seeded for 24 hours in 6-well plates and further treated in the absence (control) or presence of 25 mM or 50 mM sorbitol for 4 hours. The mitochondrial transmembrane potential, $\Delta\Psi m$ (TMRM/MTG), mitochondrial ROS production (DHR/MTG), superoxide (HE/MTG), H_2O_2 (DCF/MTG), and GSH (MCB/MTG) were measured by flow cytometry. Data represent mean ± SEM of mean fluorescent intensity (MFI) values of 5 experiments. Statistical analyses were performed with two-tailed t-test. Brackets indicate differences between mouse strains at $p < 0.05$. **G**, Effect of sorbitol on JNK phosphorylation in 1875 TALKO hepatoma cells. 150,000 cells were seeded for 24 hours in 6-well plates and further treated in the absence (control) or presence of 25 mM, 50 mM, 100 mM, 200 mM, 300 mM, 400 mM, or 500 mM sorbitol for 30 minutes. pJNK levels (Cell Signaling Technology Cat. No. 4668) were assessed relative to β-actin (Millipore Cat. No. Mab1501R) using western blot. Upper panel, representative western blot. Lower panel, cumulative analysis of dose-dependent pJNK activation by sorbitol. Values are expressed as fold changes relative to the mean of control cells set at 1.0. Data represent mean ± SEM of 5 experiments. Statistical analysis was performed with two-tailed t-test. *, $p < 0.05$ relative to control. **H**, Effect of sorbitol on proliferation of 1875 TALKO hepatoma cells. 2,500 cells were seeded for 24 hours in 6-well plates. After washing the wells twice with PBS, fresh medium was added to each well with or without (control) sorbitol for 4, 8, or 12 more hours and cellular DNA content was measured using the CyQUANT Cell Proliferation Assay (ThermoFisher Cat. No. C7026). Data represent mean ± SEM of CyQUANT fluorescence values of 5 experiments. Statistical analysis was performed with two-tailed t-test. Brackets indicate differences relative to control at $p < 0.05$.

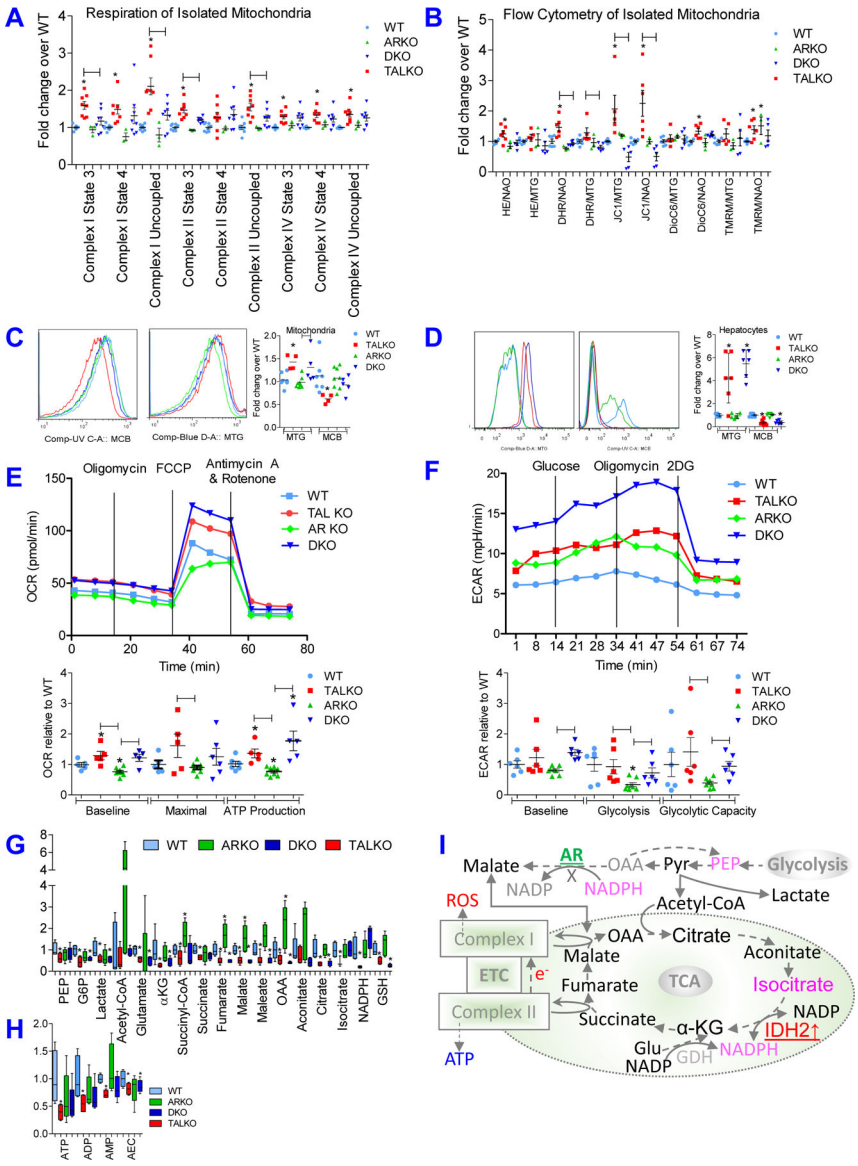

Figure 6. AR inactivation limits mitochondrial ETC activity at complex I and ROI production without affecting the accumulation of mitochondria, ATP synthesis or glycolytic capacity in TAL-deficient hepatocytes.

A, Cumulative analyses of O_2 consumption rates (OCR) through ETC complexes I, II, and IV. During the assay of each ETC complex, 150 uM ADP and 150 uM Pi were added to attain state 3 respiration; when the ADP has been exhausted state 4 respiration was attained; after achieving a stable rate for state 4 respiration, 2uM mClCCP was added to measure uncoupled O_2 consumption, which is an indicator of maximal ETC capacity. In all experiment, O_2 consumption was normalized to that of the WT control strain, which was studied in parallel and set at 1.0 for each ETC complex. Mitochondria were isolated from WT (n=8), TALKO (n=8), ARKO (n=3), and 8 DKO mice (n=8). Data represent mean ± SEM. Using two-tailed t-test, differences at $p < 0.05$ relative to WT are indicated by *; differences at $p < 0.05$ between other mouse strains are indicated by brackets. **B**, Measurement of ROI production (by HE and DHR fluorescence) and ΔΨm (by JC-1,

DiOC6, and TMRM fluorescence) relative to mitochondrial mass (by NAO and MTG fluorescence) using flow cytometry. Mitochondria were isolated from WT (n=8), TALKO (n=8), ARKO (n=3), and 8 DKO mice (n=8). Data represent mean ± SEM. Using two-tailed t-test, differences at $p < 0.05$ relative to WT are indicated by *; differences at $p < 0.05$ between other mouse strains are indicated by brackets. **C**, Measurement of mitochondrial mass (by MTG fluorescence) and GSH in isolated mitochondria (MCB fluorescence). Mitochondria were isolated from 7 WT, 4 TALKO, 8 ARKO, and 5 DKO mice. Data represent mean ± SEM. **D**, Measurement of mitochondrial mass (by MTG fluorescence) and GSH in isolated hepatocytes (by MCB fluorescence) from 6 WT, 6 TALKO, 6 ARKO, and 6 DKO mice. Data represent mean ± SEM. **E**, Measurement of mitochondrial respiration via OCR by isolated hepatocytes from WT (n=5), TALKO (n=5), ARKO (n=8), and DKO mice (n=5). Data represent mean ± SEM. Left panel shows representative tracings from WT, TALKO, ARKO, and DKO mice recorded in parallel. Right panel shows cumulative analysis of baseline and maximal respiration and mitochondrial ATP production. **F**, Assessment of glycolytic activity by extracellular acidification rates (ECAR). Left panel shows representative tracings from WT, TALKO, ARKO, and DKO mice recorded in parallel. Right panel shows cumulative analysis of baseline ECAR, glycolysis rate, and glycolytic capacity from WT (n=6), TALKO (n=6), ARKO (n=8), and DKO mice (n=6). Data represent mean ± SEM. **G**, Steady-state levels of glycolysis and TCA metabolites in liver extracts of age-matched female WT, TALKO, ARKO, and DKO mice, using ≥ 4 mice per strain. Data represent mean ± SEM. **H**, Assessment of ATP, ADP, AMP and adenylate energy charge (AEC) calculated according to the Atkinson formula ($AEC = ([ATP] + 0.5[ADP])/([ATP] + [ADP] + [AMP])$) [40] in liver extracts of age-matched female WT (n=5), TALKO (n=4), ARKO (n=5), and DKO mice (n=5). Data represent mean ± SEM. **I**, Schematic diagram of TCA cycle and glycolytic substrates that shuttle between mitochondria and the cytosol and transport reducing power. NADPH can be regenerated from NADP by oxidation of glutamate, isocitrate, malate, and oxaloacetate by GDH, IDH2, ME, and AR. The TCA cycle may operate in the forward direction, which supports electron transport and ATP production and involves NADPH production by IDH2. In the reverse reaction, IDH2 depletes NADPH.

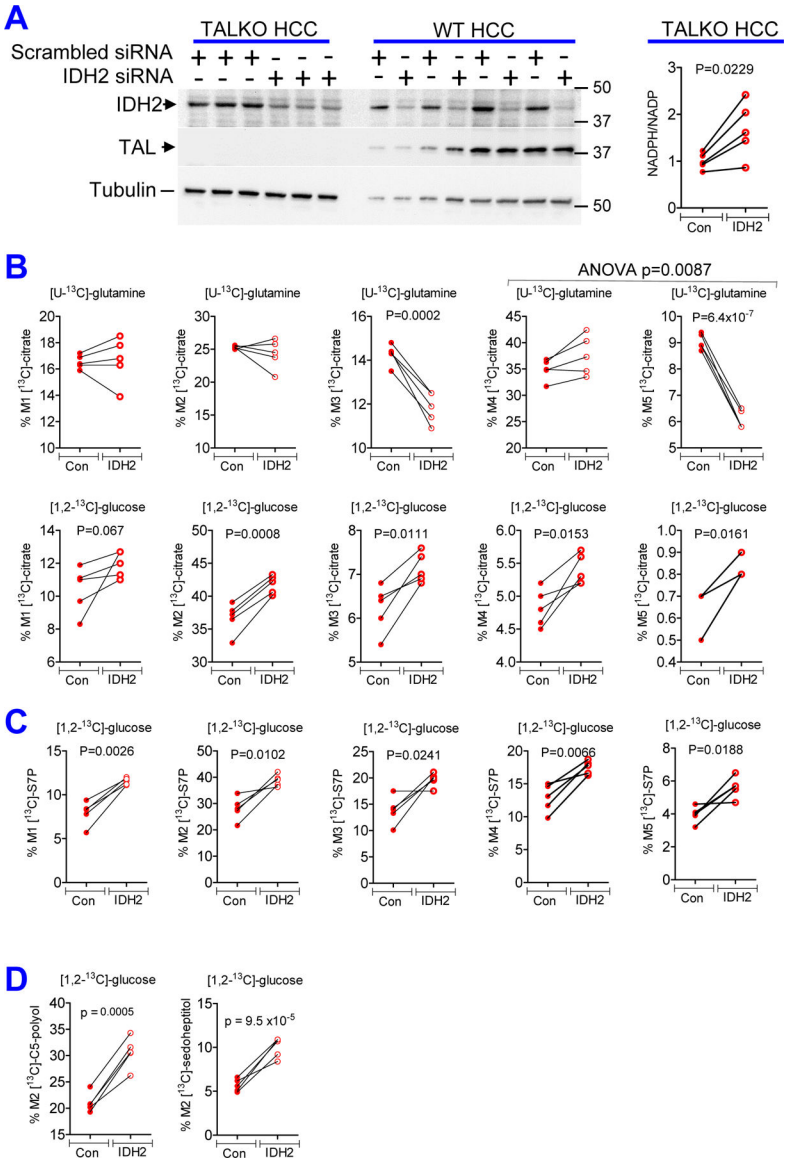

Figure 7. Effect of siRNA-mediated knockdown of IDH2 on metabolic flux through the TCA cycle and the PPP in 1875 TALKO hepatoma cells.

The data represent five independent experiments. P values reflect statistical analyses performed with two-tailed t-test in all panels. **A,** Left panels, Western blot detection of IDH2, TAL, and tubulin loading control in TALKO and WT HCC cell lines (ATCC CRL-2717 and ATCC CRL-2712). IDH2 was detected with mouse monoclonal antibody (Invitrogen catalogue number MA5–17271); TAL was detected with rabbit antibody 169 [65], tubulin was detected with rabbit monoclonal antibody (Cell Signaling catalogue number CST 2128L). Right panel, NADPH/NADP ratio was determined in 1875 TALKO cells treated with scrambled (Con) or IDH2 siRNA. P value represents comparison with two-tailed paired t-test of four independent experiments. **B,** Effect of IDH2 knockdown on enrichment of [M1-^{13C}]-citrate, [M2-^{13C}]-citrate, [M3-^{13C}]-citrate, [M4-^{13C}]-citrate, and [M5-^{13C}]-citrate in 1875 TALKO hepatoma cells labelled with [1, 2-^{13}C]-glucose (CLM-504–0.5, Cambridge Isotope Laboratories; Cambridge, MA) or [U-^{13}C]-glutamine

(DLM-1150–0.5, Cambridge Isotope Laboratories; Cambridge, MA) for 24 hours. **C**, Effect of IDH2 knockdown on enrichment of [M1-^{13C}]-S7P, [M2-^{13C}]-S7P, [M3-^{13C}]-S7P, [M4-^{13C}]-S7P, [M5-^{13C}]-S7P, and [M6-^{13C}]-S7P, in 1875 TALKO hepatoma cells labelled with [1, 2-^{13}C]-glucose (CLM-504–0.5, Cambridge Isotope Laboratories; Cambridge, MA) for 24 hours. **D**, Effect of IDH2 knockdown on the accumulation of [M2-^{13}C]-sedoheptitol and [M2-^{13}C]-C5-polyols in [1, 2-^{13}C]-glucose-labelled TALKO hepatoma cells.